Volume 17
Number 11
21 March 2025
Pages 6187-6900

Nanoscale

rsc.li/nanoscale

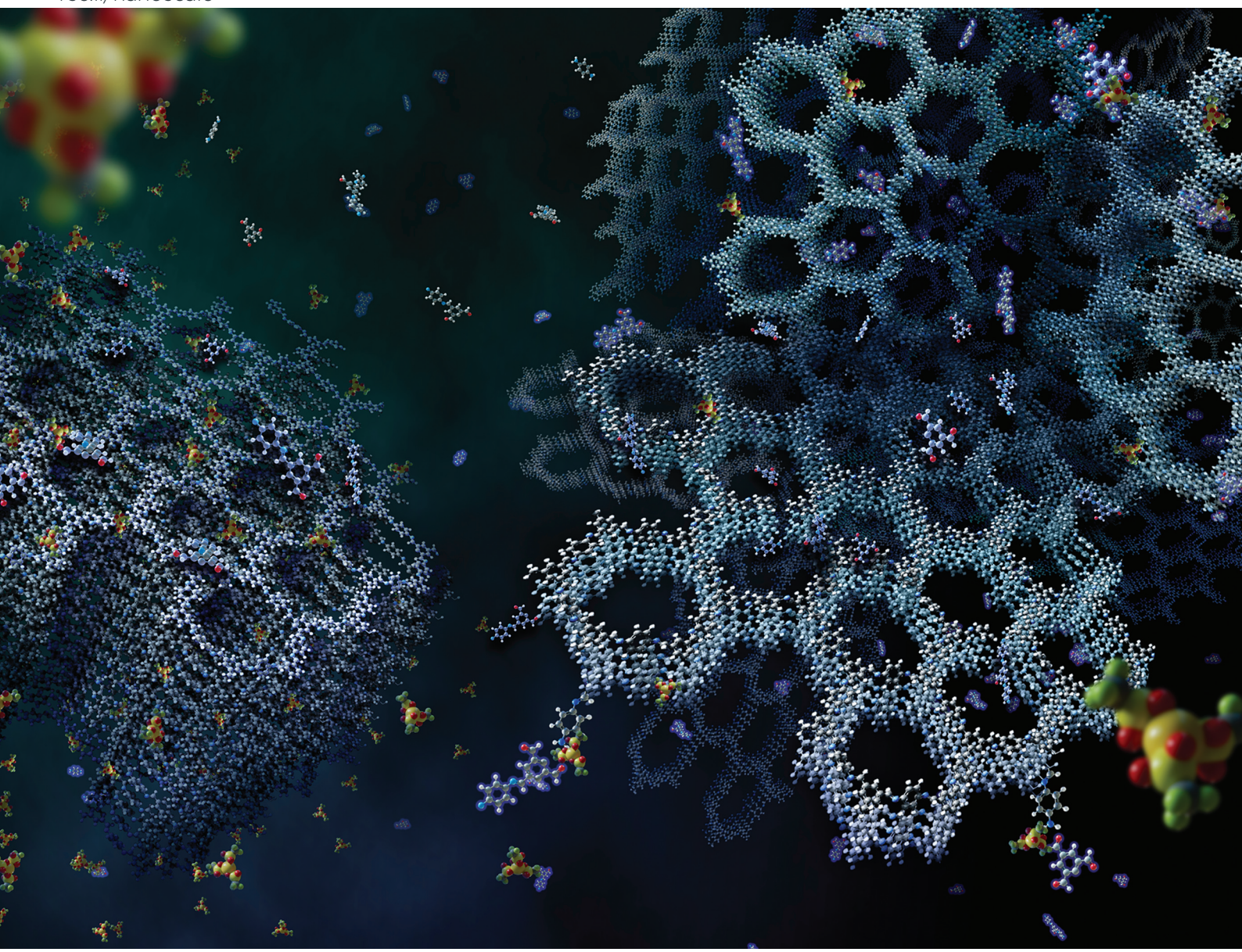

ISSN 2040-3372

ROYAL SOCIETY OF CHEMISTRY

PAPER
Mark A. Snyder *et al.*
Catalyst-derived hierarchy in 2D imine-based covalent organic frameworks

NCNST

Nanoscale

ROYAL SOCIETY OF CHEMISTRY

PAPER

View Article Online
View Journal | View Issue

Cite this: *Nanoscale*, 2025, **17**, 6488

Catalyst-derived hierarchy in 2D imine-based covalent organic frameworks†

Hao Guo, [a] Joseph P. Cline,[b] Ryan Thorpe,[c] Christopher J. Kiely,[a,b,c] Srinivas Rangarajan [a] and Mark A. Snyder *[a]

Received 11th November 2024,
Accepted 15th January 2025

DOI: 10.1039/d4nr04717f

rsc.li/nanoscale

Identifying facile strategies for hierarchically structuring crystalline porous materials is critical for realizing diffusion length scales suitable for broad applications. Here, we elucidate synthesis–structure–function relations governing how room temperature catalytic conditions can be exploited to tune covalent organic framework (COF) growth and thereby access unique hierarchical morphologies without the need to introduce secondary templates or structure directing molecules. Specifically, we demonstrate how scandium triflate, an efficient catalyst involved in the synthesis of imine-based COFs, can be exploited as an effective growth modifier capable of selectively titrating terminal amines on 2D COF layers to facilitate anisotropic crystal growth. We systematically map a compositional pseudo-phase space and uncover key mechanistic insights governing the catalyst-derived evolution of globular COFs with sub-micron diffusion length scales into unique rosette structures. Comprised of interconnected, high-aspect-ratio crystalline porous sheets of only several unit cells in thickness, the resulting COFs offer orders of magnitude reduction in diffusion length scales and several-fold increase in external surface area, enabling rapid uptake of bulky dyes. Generally, the resulting synthesis–structure–function relations hold promise for realizing unique control over COF mesostructure, morphology, and function.

Introduction

Covalent organic frameworks (COFs) are a burgeoning class of crystalline porous materials formed by the reticulation of building block molecules into two- (2D) or three-dimensional (3D) porous organic networks.[1–3] Owing to the intrinsic stability[4,5] and tunable functionality[6] of the covalently bonded framework, and the ability to design building block structure and chemistry to tailor pore topology and size,[1,7] COFs show promise in a wide range of applications, including in adsorption,[8] catalysis,[9] separations,[10] and chemical sensing,[11] among others.[12] Such applications commonly rely on efficient molecular access to pore topologies.[13–15] However, larger particle sizes, required for ease of processing in practical applications, offer characteristic diffusion length scales that stymie access to the intracrystalline pores. This is especially true in cases where diffusion becomes sluggish as pore diameters approach molecular dimensions.

Efforts to overcome transport limits in crystalline porous materials have focused on strategies for introducing pore hierarchy to facilitate molecular access of the smallest pores deep within a particle. For example, strategies for the hierarchical structuring of zeolites,[16] a class of crystalline microporous materials[17,18] with pore topologies analogous to some COFs, have included post-synthetic processing (*e.g.*, etching)[19] and sacrificial templating[20,21] resulting in embedment of mesopores within the microporous framework. Additional elegant strategies have employed designer surfactants and organic structure-directing agents[22–24] or taken advantage of crystal twinning and defects[25,26] as a means for growing intrinsically hierarchical zeolites.

2D COFs have a wider range of accessible pore sizes than zeolites, classifying them among microporous to mesoporous (*ca.* 5 Å to 5 nm) materials.[27,28] Despite the wide range of

[a]*Dept. of Chemical and Biomolecular Engineering, Lehigh University, Bethlehem, PA 18015, USA. E-mail: snyder@lehigh.edu*
[b]*Dept. of Materials Science and Engineering, Lehigh University, Bethlehem, PA 18015, USA*
[c]*Institute for Functional Materials and Devices, Lehigh University, Bethlehem, PA 18015, USA*

† Electronic supplementary information (ESI) available: Morphology of COFs synthesized under different amounts of acetic acid and a low concentration of 0.002 eq. $Sc(OTf)_3$; reproducibility of COFs synthesized under different catalytic conditions and different reaction times; FTIR comparisons of as-made COFs, monomers, solvents, and $Sc(OTf)_3$ catalyst; $Sc(OTf)_3$ dispersion in COF-LZU1 agglomerated particles; quantified elemental analysis of as-made COFs; crystallographic indexing of as-made COFs, reaction time sensitivity, and estimation of edge amines; DFT simulation of alternative metal triflate binding to COF framework; morphology, composition, and crystallinity of as-made COF-LZU1 under 0.02 eq. $Sc(OTf)_3$ with added DI water; retention of morphology with activation; pore size changes with introduction of defects; hierarchical COF literature comparison; RdB and MB adsorption equilibrium time. See DOI: https://doi.org/10.1039/d4nr04717f

nominal COF pore sizes, transport limits remain a persistent challenge due to the common micrometer particle sizes and concomitantly large characteristic diffusion length scales,[29] pore restrictions deriving from the shifting of 2D COF sheets from eclipsed to staggered positions,[30,31] and the growing interest in deploying COFs for processing of larger molecules (*e.g.*, per- and polyfluoroalkyl substances – PFAS,[32,33] other organic pollutants,[34–36] bulky polysaccharides,[37] *etc.*) that approach the size of COF pores. To circumvent transport limits in COFs, studies have employed judicious selection of building blocks to optimize pore size and chemistry[32] and have focused on avoiding undesired pore restrictions by ensuring highly crystalline eclipsed stacking of 2D COF layers.[38,39]

In cases where the pore size is commensurate with molecular dimensions, strategies for hierarchically structuring COFs have been analogous to those used for zeolites.[40–45] Sacrificial templating has led to COFs with meso to macroscale pores embedded within the COFs upon template removal,[43,44] whereas *in situ* templating of macrostructured COFs has been achieved by adding foaming agents during COF crystallization.[42] Separately, growth modifiers, building blocks with reduced functionality, have been introduced to control growth kinetics and realize structural hierarchy comprising thin interconnected COF sheets.[46] Several studies have separately demonstrated how concentration-sensitive dimerization or temperature-dependent decomposition of specialized monomers can be employed for tuning COF morphology among globular, intrinsically hierarchical, or mesopore-etched structures.[41,45]

Dichtel and coworkers[47–49] and others[46,50] have extensively studied covalent linkage kinetics and synthetic catalysts with the goal of maximizing crystallinity by minimizing the defects of 2D imine-based COFs. Here, drawing inspiration from the elegant hierarchical structuring of zeolites, we explore the opposite scenario of how crystalline defects—induced by catalytic control of the covalent linkage kinetics—can be exploited for synthesizing intrinsically hierarchical COFs at room temperature and with facile and scalable strategies, namely without the need to introduce secondary templates or structure directing molecules. Specifically, we develop synthesis–structure–function relations linking catalyst type and composition to product morphology for representative 2D imine-based COFs, COF-LZU1 and TAPB-PDA. We show how scandium triflate, $Sc(OTf)_3$, an alternative to acetic acid that is traditionally used in the synthesis of imine-based COFs, not only acts as an efficient catalyst but also tunes framework defects and appears to mediate anisotropic COF growth. The unique rosette-structured COFs that result bear interdigitated, planar features of only tens of nanometers in thickness, offering several fold higher external surface areas, orders of magnitude shorter characteristic diffusion lengths, and more accessible pores compared with globular forms of the same COFs synthesized under different catalytic conditions. The hierarchical structure and concomitant enhanced external surface area and expanded direct access to COF pores result in faster uptake of, and higher capacity for, bulky dyes.

Experimental

Chemicals

All chemicals were purchased from commercial vendors and used without further purification, including 1,3,5-Triformylbenzene (TFB, Thermo Scientific Chemicals, 98%), 1,4-Diaminobenzene (DAB, Sigma, 98%), 1,3,5-Tris(4-aminophenyl)benzene (TAPB, AmBeed, 97%), Terephthaldehyde (PDA, Sigma, 99%), Scandium triflate ($Sc(OTf)_3$, Sigma, 99%), glacial acetic acid (Sigma, 99%), dioxane (Sigma, 99%), mesitylene (Sigma, 98%), methanol (Sigma, 99%), Rhodamine B (RdB, Sigma, <100%), and Methylene blue (MB, Sigma, <100%).

COF-LZU1 synthesis

COF-LZU1 was synthesized from 1,3,5-Triformylbenzene (TFB) and 1,4-Diaminobenzene (DAB) using either acetic acid or $Sc(OTf)_3$ as catalysts. In a typical synthesis 0.31 mmol of TFB and 0.46 mmol of DAB were added to a 20 mL scintillation vial under N_2 protection and charged with 6.2 mL dioxane/mesitylene solution (4 : 1, v/v). The catalyst solution was prepared in a separate scintillation vial. In the case of acetic acid, a prescribed volume of 10.5 M aqueous acetic acid (0.44, 1.32, 3.09, 4.85, 6.17 mL) was added to 6.2 mL dioxane/mesitylene solution (4 : 1, v/v) to achieve 5, 15, 35, 55, and 70 eq. of acetic acid, respectively, relative to amine groups of DAB. Additionally, a water-free synthesis was carried out with a catalyst solution comprising 0.26 mL of glacial acetic acid in 6.2 mL dioxane/mesitylene solution (4 : 1, v/v), corresponding to 5 eq. acetic acid. In the case of $Sc(OTf)_3$, prescribed amounts of the catalyst (0.9, 9.1, 18.2, and 41.0 mg) were dissolved in 6.2 mL dioxane/mesitylene solution (4 : 1, v/v) to achieve 0.002, 0.02, 0.04, and 0.09 eq. of $Sc(OTf)_3$, respectively, relative to amine groups of DAB. The monomer solutions and catalyst solutions were sonicated separately at room temperature until the monomers and catalysts fully dissolved (*i.e.*, 1–2 min). Catalyst solutions were added to the monomer solutions and vigorously stirred for 1 h at room temperature. Precipitates from the reaction were isolated by centrifugation at 10 000 rpm for 10 min, followed by washing with reaction solvents (dioxane/mesitylene, 4 : 1, v/v) and vacuum filtration (Fisher Scientific, Q5 filter paper with 2–5 μm particle retention). The recovered wet powders were dried by rotary evaporation at 40 °C for 1 h.

TAPB-PDA synthesis

TAPB-PDA was synthesized from 1,3,5-Tris(4-aminophenyl) benzene (TAPB) and Terephthalaldehyde (PDA) using either acetic acid or $Sc(OTf)_3$ as catalysts. In a typical synthesis, 0.23 mmol of TAPB and 0.34 mmol of PDA were added to a 20 mL scintillation vial under N_2 protection followed by addition of 4.6 mL dioxane/mesitylene solution (4 : 1, v/v). The catalyst solution was prepared in a separate scintillation vial. In the case of acetic acid, a prescribed volume of 10.5 M acetic acid in water (0.33, 1.3, 2.28, 3.58 mL) was added to 4.6 mL dioxane/mesitylene solution (4 : 1, v/v) to achieve 5, 20, 35, and 55 eq. of acetic acid, respectively, relative to amine groups of

TAPB. $Sc(OTf)_3$ solutions were prepared by addition of prescribed amounts of the catalyst (0.67, 6.7, 30.2, 50.4 mg) to 4.6 mL dioxane/mesitylene solution (4 : 1, v/v) to achieve 0.002, 0.02, 0.09, and 0.15 eq. of $Sc(OTf)_3$, respectively to amine groups of TAPB. The monomer and catalyst solutions were sonicated and combined as described for COF-LZU1, but the reaction was carried out for 24 h before the same washing, recovery, and drying steps.

Activation of COF-LZU1

Activation of COF-LZU1 for dye adsorption requires the removal of residual solvents and $Sc(OTf)_3$. Residual dioxane and mesitylene were removed from as-made dried powders of COF-LZU1 by dispersion of the powders (50 mg) in 45 mL of methanol, followed by sonication for 20 min, vacuum filtration, and rotary evaporation of the recovered wet powders at 40 °C for 30 min. The resulting powders are referred to as "methanol-washed COF-LZU1". $Sc(OTf)_3$ was fully removed from the methanol-washed COF-LZU1 powders by sonication in 45 mL DI water for 20 min followed by vacuum filtration. Finally, the resulting wet powders were dispersed by sonication for 1 min in water and soaked at room temperature for *ca*. 10 h before recovery by filtration and drying by rotary evaporation at 40 °C for 1 h. This water dispersion, soaking, and drying process was repeated once to obtain fully activated COF-LZU1 powders.

Instrumentation and characterization

Scanning electron microscopy. Powder samples were imaged with a Hitachi 4300 Scanning Electron Microscope (SEM) at 5 kV. All samples were sputter-coated (40 s) with Iridium before imaging to improve conductivity and image quality.

Transmission electron microscopy. Transmission Electron Microscopy (TEM) images were collected using a JEOL JEM2100 operating at an accelerating voltage of 200 kV. Samples for TEM analysis were prepared by drop casting COF suspensions (0.02 g L^{-1} in 4 : 1 (v/v) dioxane/mesitylene) onto an ultra-thin holey carbon film supported on a copper mesh (150 μm) TEM grid (Electron Microscopy Science, HC400-Cu-150) followed by overnight vacuum drying.

Fourier-transform infrared spectroscopy. Fourier-Transform Infrared (FTIR) spectra were collected at room temperature on powder samples using a Thermo Scientific Nicolet iS 10 FTIR spectrometer with a Thermo Smart iTX ATR optics module.

Energy dispersive X-ray spectroscopy. Energy Dispersive X-ray Spectroscopy (EDS) was conducted on an aberration-corrected JEOL JEM-ARM200CF transmission electron microscope (STEM) equipped with a high angle annular dark field (HAADF) detector and a Centurion X-ray energy dispersive (XED) spectrometer. The microscope was operated at 200 kV in STEM mode to characterize elemental spatial distribution. The sample preparations were the same as the TEM samples.

X-ray photoelectron spectroscopy. Powder samples were affixed by copper tape to a sample plate, and X-ray Photoelectron Spectroscopy (XPS) measurements were carried out on a custom-built SPECS NAP-XPS system equipped with a monochromated XR50MF Al Kα X-ray source which produced a beam of 1486.6 eV photons. Electrons were detected with a Phoibos 1D-DLD hemispherical analyzer with an acceptance angle of 44° and a mean analyzer radius of 150 mm. The angle between the X-ray source and detector was fixed at 54.7°. Survey spectra were acquired at a pass energy of 70 eV and core-level spectra were acquired at a pass energy of 20 eV. Charge neutralization during the analysis was established with a beam of 2 eV operated at a current of 20 μA. The binding energy was calibrated using the adventitious carbon peak at 284.8 eV. Core-level data was treated by subtracting a Shirley-type background and then fitting with pseudo-Voigt profiles which generally consisted of 80% Gaussian and 20% Lorentzian components. Atomic percentages were calculated by normalizing the area of core level peaks by their Scofield sensitivity factors and their inelastic mean free path, as estimated by the $KE^{0.6}$ approximation.

Powder X-ray diffraction. Powder X-ray Diffraction (PXRD) patterns were collected at room temperature from dried COF powders using a Panalytical Empyrean XRD at 45 kV and 20 mA. Baselines were further subtracted using HighScore XRD analysis software with bending factor of 0 and granularity of 10. Materials Studio was used to compute theoretical diffraction patterns based on CIF files obtained from the Materials Cloud database[51] for COF-LZU1 and TAPB-PDA in their eclipsed form. Additionally, Pawley refinement was employed to interpret diffraction patterns collected on as-made COFs.

Low-energy ion scattering. Low-energy Ion Scattering (LEIS) was conducted on powder samples using an ION-TOF Qtac[100] equipped with a toroidal analyzer. The surface of the sample was bombarded with 3 keV He^+ operated at a current of 5 nA and a raster area of 1 mm^2. The double toroidal analyzer accepted ions at a scattering angle of 145 degrees with respect to the incident beam across all azimuthal angles. The sputter beam was 0.5 keV Ar^+ operated at a current of 100 nA and a raster area of 4 mm^2. At each step in the depth profile, the analysis and sputter beam doses were $5e^{14}$ He^+ per cm^2 and $1.5e^{15}$ Ar^+ per cm^2, respectively. This corresponds to a depth of approximately 3 nm per sputter cycle. Charge neutralization was performed using a 12 V electron beam operated at a current of 4 μA. The percentage of all elements was calculated by subtracting linear backgrounds and normalizing the peak areas by their empirically calculated sensitivity factors.

Gas adsorption. Nitrogen physisorption analysis was performed on a Micromeritics ASAP 2020 instrument under liquid nitrogen conditions (77 K). Prior to measurements, samples were degassed at 120 °C under 6 μmHg vacuum for 24 h. Low N_2 dosing (2 cc per dose) was employed until the relative pressure $P/P_0 = 1.05 \times 10^{-4}$ was reached after which measurements of adsorption and desorption branches were made according to a pressure table. Total surface areas were calculated by applying the Brunauer–Emmett–Teller (BET) method. Cumulative surface areas and cumulative pore volumes were obtained from the adsorption branch by applying the non-local density functional theory (NLDFT) method specifically with the N_2 – Cylindrical Pores – Oxide Surface

model.[48] The micropore surface area (S_{micro}) and micropore volume (V_{micro}) were computed based on the cumulative surface area and cumulative pore volume, respectively, associated with pores of up to 20 Å in diameter. The defected surface area (S_{defect}) and defected volume (V_{defect}) was computed from the cumulative surface area and cumulative pore volume, respectively, associated with pores between 20 Å and 25 Å in diameter. The external surface area ($S_{external}$) and external volume ($V_{external}$) was computed from the cumulative surface area and cumulative pore volume, respectively, associated with pores greater than 25 Å in diameter.

Room temperature dye uptake experiments. Aqueous stock solutions of Rhodamine B (RdB; 0.25 mM, 0.5 mM) and Methylene blue (MB; 0.25 mM, 0.5 mM) were prepared and kept in the dark. UV-Vis absorbance measurements at 555 nm (Rhodamine B) or 664 nm (Methylene blue) were carried out at room temperature on a Shimadzu UV-2600 spectrophotometer under kinetic mode. Absorbance-concentration calibration curves for each dye were made using solutions of concentrations up to *ca.* 0.05 mM for Rhodamine B and 0.01 mM for Methylene blue. Dye uptake experiments were carried out in 20 mL scintillation vials by dispersing 10 mg of activated COF-LZU1 in 8 mL DI water *via* sonication for 1 min. The vials were covered with aluminum foil and injected with 2 mL of the 0.25 mM or 0.5 mM stock dye solutions under stirring for initial dye concentrations of 0.05 mM and 0.1 mM, respectively. Dye uptake was measured by quantification of the concentration of unadsorbed dye (C_t [mM]) *via* UV-Vis absorbance measurement of supernatant samples that were periodically extracted from the system between 30 min and 48 h. Specifically, 1 mL aliquots of the uptake solutions were extracted and microcentrifuged at 17 000*g* for 5 min. Duplicate portions of the resulting supernatant, $V_{measure}$, were diluted with DI water into the calibration range, and UV-Vis absorbance was measured. The remaining solution was sonicated to redisperse the pelletized COF and returned to the uptake solution. Dye uptake at the time of the n^{th} aliquot (Q_{tn} [mmol g^{-1}]) was calculated according to eqn (1),

$$Q_{tn} = \frac{[V_0 - (n-1) \times V_{measure}] \times (C_0 - C_{tn}) + \sum_{a=1}^{a=n-1} V_{measure} \times (C_0 - C_{ta})}{m_{COF}} \quad (1)$$

where V_0 [mL] is the starting volume of the uptake solution (10 mL), C_0 [mM] is the initial dye concentration in the uptake solution, C_{tn} [mM] is the concentration of dye for the n^{th} aliquot, and m_{COF} is the mass of the activated COF-LZU1 powder (*ca.* 10 mg).

Room temperature dye isotherm experiments. 10 mg of activated COF-LZU1 synthesized under various conditions was dispersed by sonication in 8 mL DI water in 20 ml scintillation vials. Vials were covered with aluminum foil, and 2 mL of stock dye solutions of specified concentration (RdB: 0.25, 0.5, 0.75, 1.0, 1.25, and 1.5 mM; MB: 0.5, 1.0, 1.5, 2.0 mM) were added to realize starting concentrations of *ca.* 0.05–0.3 mM RdB and 0.1–0.4 mM MB. Dye adsorption was carried out under stirring for 96 h in the case of RdB and 120 h in the case of MB, after which the supernatant was extracted by microcentrifugation. The resulting equilibrium concentration of unadsorbed dye (C_e [mM]) was measured by UV-Vis, and the corresponding equilibrium uptake, Q_e, was calculated according to eqn (2),

$$Q_e = \frac{V_0 \times (C_0 - C_e)}{m_{COF}} \quad (2)$$

where V_0 [mL] is the volume of the uptake solution (10 mL), C_0 [mM] is the initial dye concentration, and m_{COF} is the mass of COF (10 mg). Adsorption affinities (K_L [mM^{-1}]) and capacities (Q_m [mmol g^{-1}]) were derived from fitting the Langmuir equation (eqn (3)) to the results.

$$Q_e = \frac{Q_m \times K_L \times C_e}{C_e \times K_L + 1} \quad (3)$$

The maximum specific loading of a dye on the external surface area of a given COF, $L_{max|EXT}$[mmol g^{-1}], was calculated according to eqn (4),

$$L_{max|EXT} = S_{external}/S_{dye} \quad (4)$$

under the assumption of monolayer adsorption. S_{dye} is the area occupied by a single dye molecule (S_{RdB} = 8.16 × 10^5 m^2 mol^{-1}, S_{MB} = 3.84 × 10^5 m^2 mol^{-1}), estimated as the product of the kinetic diameter and the longest dimension of the dye molecule.

Density-functional theory (DFT) simulations of Sc(III)-COF coordination. All calculations were carried out using plane wave periodic density functional theory (DFT) code Vienna *Ab initio* Simulations Package (VASP).[52] A tri-layer slab of COF-LZU-1 (with a 1 × 1 unit cell in the *x* and *y* directions) with at least 15 Å of vacuum in the third direction was used to model a multi-layered COF nanoparticle. All calculations were done using the Projector Augmented Wave (PAW) potentials with the generalized gradient approximation (GGA) Perdew–Burke–Erzenhof (PBE)[53] exchange-correlational functional with a D3 dispersion correction.[54–56] An energy cutoff of 550 eV was applied with an SCF convergence criterion of 10^{-5} eV as well as a force-convergence criterion of 0.02 eV A^{-1}. Gaussian smearing was applied with a spread of 0.05 eV and a Gamma point K-point sampling was used (due to the large unit cell size). Calculations involving the gas phase (*e.g.*, metal triflates, $M(OTf)_x$; M : Sc as well as Yb and Zn) were carried out using identical settings in a box with at least 10 Å of vacuum in all directions. The binding energy (BE) of the triflate onto a site (physisorbed or chemisorbed) was generally calculated as:

$$BE = E_{COF+M(OTf)_x} - E_{COF} - E_{M(OTf)_x} \quad (5)$$

where $E_{COF+M(OTf)_x}$ is the energy of COF with the triflate adsorbed, E_{COF} is the energy of COF, and $E_{M(OTf)_x}$ is the energy of triflate. BEs, by definition, are negative; a more negative

binding energy value implies stronger adsorption of the triflate.

Results and discussion

We selected COF-LZU1 and TAPB-PDA from the array of established 2D imine-based structures to elucidate how synthetic catalysts might be exploited generally to tailor morphology, and, thereby, the characteristic diffusion length scale. These two imine-based COFs exhibit hexagonal pores and were chosen due to their room-temperature synthesis relative to the solvothermal processing common among other non-hexagonal COFs (*e.g.*, triangular HPB-COF;[57] rhombic TAPPy-PDA[58] and Py-DHPh/Py-BPyPh;[59] pentagonal TAPP-PBTD-COF;[60] bi-porous PT-COF[61]). The comparable synthesis routes for COF-LZU1 and TAPB-PDA COFs are depicted in Scheme 1, wherein room temperature reticulation is achieved with distinct monomer combinations in conventional dioxane/mesitylene solvents for reaction times resulting in maximum crystallinity.[47,62] With the dioxane/mesitylene solvent ratio held fixed throughout this work at the 4 : 1 (v/v) ratio employed broadly in the 2D imine-based COF literature, we studied two common synthesis catalysts, acetic acid and $Sc(OTf)_3$, exploring sensitivities of COF chemistry, morphology, and functionality to catalyst concentration. We focused on $Sc(OTf)_3$ as an alternative to acetic acid because of its identification from among a range of metal triflates (*e.g.*, Sc, Eu, In, Yb, Y, Zn) as the most efficient triflate-based transimination catalyst leading to highly crystalline 2D imine-base COF products.[47]

Catalyst sensitivity of COF morphology

Fig. 1 shows scanning electron microscopy (SEM) and transmission electron microscopy (TEM) images of the COF-LZU1 and TAPB-PDA products resulting from acetic acid or $Sc(OTf)_3$ catalytic conditions. Consistent with earlier literature reports,[63] acetic acid-based synthesis of COF-LZU1 results in globular particles (Fig. 1a). Such globular morphology persists for syntheses at low to high acetic acid concentrations (Fig. S1†). The alternative use of a nominally low concentration ($\leq$0.02 eq., Fig. 1b and S1†) of $Sc(OTf)_3$ catalyst[47] results in strikingly hierarchical rosette-like particles. Upon increasing the concentration of $Sc(OTf)_3$, the rosette-like features become less pronounced, appearing as more subtle surface roughness (Fig. 1c), with final emergence of fully globular structures at the highest $Sc(OTf)_3$ concentrations studied (Fig. 1d). SEM imaging of the product of triplicate syntheses (Fig. S2†) confirms the reproducibility of the COF-LZU1 morphological evolution as well as characteristic particle size with catalyst type and concentration. Additionally, while literature reports have suggested sensitivity of particle morphology to reaction time,[64] time-series experiments reveal the robustness of the unique rosette-like COF-LZU1 morphology and characteristic particle size to reaction times spanning 1 h to 24 h (Fig. S3a†).

We observe analogous particle morphologies relative to catalytic synthesis conditions for a different 2D imine COF, TAPB-PDA (Fig. 1e–h and Fig. S1†). Namely, TAPB-PDA products tend to be globular when synthesized with acetic acid as the catalyst, but distinctly rosette-like when low concentrations of $Sc(OTf)_3$ are used. Similar to the morphological trends observed for COF-LZU1, increasing the concentration of Sc $(OTf)_3$ leads to TAPB-PDA product morphologies that evolve toward globular structures (Fig. 1h). As with COF-LZU1, SEM imaging also confirms the reproducibility (Fig. S4†) and reaction-time invariability (Fig. S3b†) of TAPB-PDA COF prepared with the nominal catalytic conditions studied here. The similarities in morphological evolution point to potential generalizability of the effects of catalyst type and concentration on 2D imine COFs.

COF composition and crystallinity relative to catalytic conditions

Fig. 2 shows the FTIR spectra collected for as-made COF-LZU1 and TAPB-PDA COFs prepared under specified catalytic conditions, with band assignments concluded in some cases from reference spectra in Fig. S5.† The strong bands at 1620 cm^{-1} for COF-LZU1, and 1595 and 1621 cm^{-1} for TAPB-PDA COF indicate imine linkage formation.[47,63] The weaker bands at 3200–3600 cm^{-1} and 1690 cm^{-1} are assigned, respectively, to

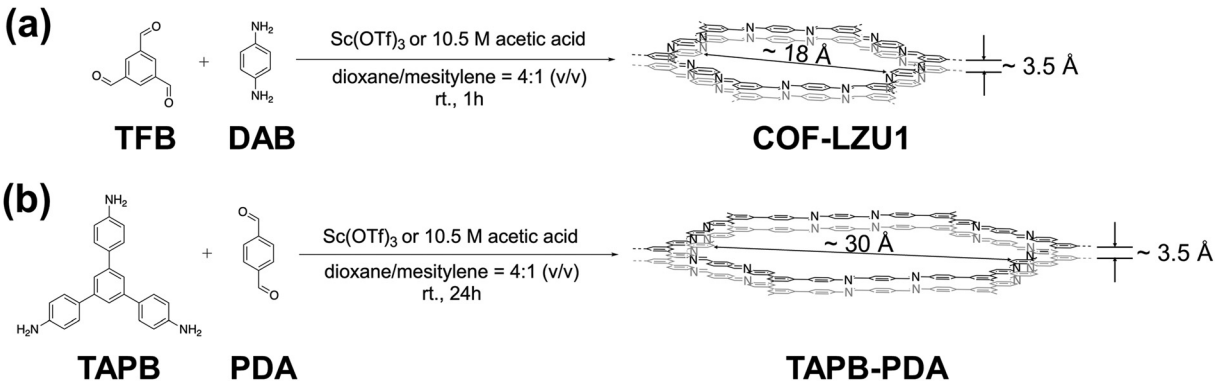

Scheme 1 Synthesis routes to (a) COF-LZU1 and (b) TAPB-PDA using either acetic acid or $Sc(OTf)_3$ as catalyst.

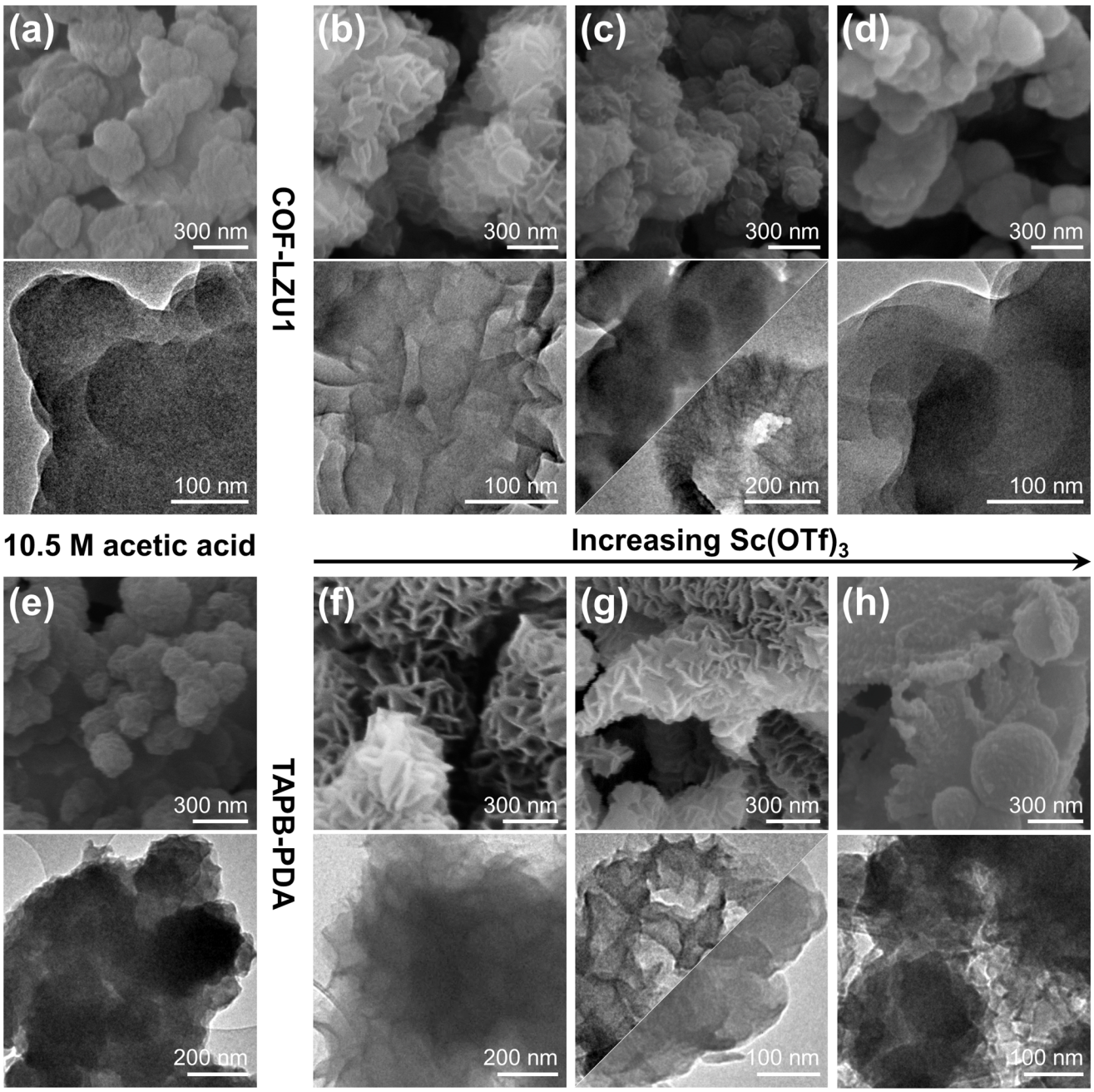

Fig. 1 SEM and TEM images of COF-LZU1 synthesized under (a) 15 eq. 10.5 M acetic acid and (b) 0.02, (c) 0.04, and (d) 0.09 eq. $Sc(OTf)_3$; and TAPB-PDA synthesized under (e) 20 eq. 10.5 M acetic acid and (f) 0.02, (g) 0.09, and (h) 0.15 eq. $Sc(OTf)_3$.

amino and formyl groups comprising terminal functionality and/or framework defects (Fig. 2c).

Bands between 2750–3100 cm^{-1} are attributable to a combination of characteristic dioxane and mesitylene peaks overlaying C–H vibrations originating from the COF framework. Further, the band at 1617 cm^{-1} is a combination of characteristic mesitylene and COF-based C–C stretching vibrations. Taken together, these spectra indicate that reaction solvents remain despite rotary evaporation at 40 °C, owing to their high boiling points (101–165 °C).

In addition to solvent occlusion within the COF framework, FTIR bands at around 1660 cm^{-1}, 1250 cm^{-1}, and 1030 cm^{-1} indicate the presence of triflate ligands as well. Specifically, the band at 1250 cm^{-1} can be assigned to both SO_3 stretches from triflate ligands and COF-based vibrations, whereas the band at 1030 cm^{-1} can be assigned to C–F stretching from the triflate ligands alone. The amount of triflate incorporated within the COFs trends qualitatively with the concentration of the catalyst used in the synthesis, as indicated by the corresponding increase in the intensity of $(OTf)_3$-associated bands.

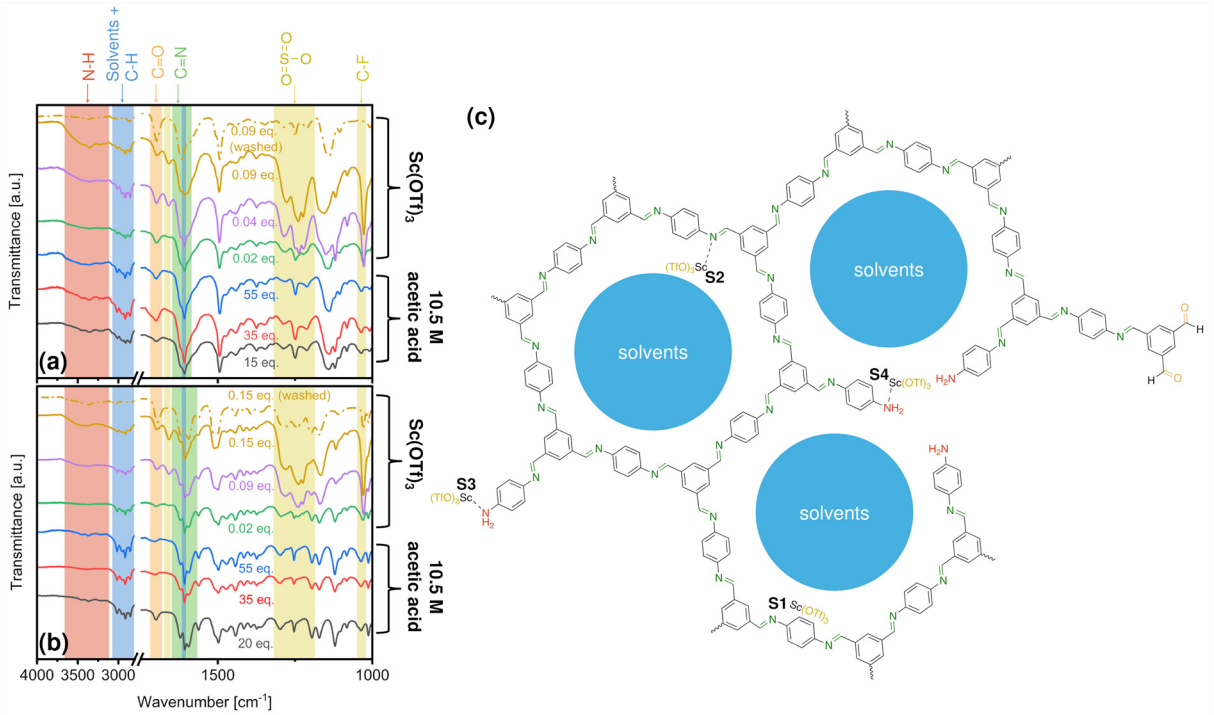

Fig. 2 FTIR spectra of as-made (a) COF-LZU1 and (b) TAPB-PDA synthesized under different catalytic conditions, with (c) molecular representation of the pores (shown for COF-LZU1) as well as possible framework defects, terminal functional groups, and potential sitings of $Sc(OTf)_3$ within the COF framework, including: (S1) physisorbed in the pores, coordinated with (S2) a framework N, (S3) a dangling terminal amine, or (S4) an amine N from a framework defect.

Separately, EDS elemental mapping (Fig. S6†), carried out on a representative COF-LZU1 sample prepared with 0.02 eq. Sc $(OTf)_3$ catalyst, reveals a uniform distribution of Sc throughout the COF-LZU1 particles, suggesting the incorporation of the full $Sc(OTf)_3$ moiety within the COF structure.

Potential siting of $Sc(OTf)_3$ in the COFs could conceivably occur *via* physisorption in the pores, or by coordination with framework imines or with amines from framework edges or defects, as depicted in Fig. 2c. Complementary XPS analysis offers critical insight into Sc incorporation during synthesis. Fig. 3 shows N 1s and Sc 2p spectra for COFs synthesized under different catalytic conditions (C 1s, S 2p, and F 1s spectra included in Fig. S7–S9†). The increasing intensity of the Sc 2p peaks (Fig. 3a and c) indicates increasing Sc incorporation with increasing catalyst concentrations in the reaction solution as quantified in Tables 1, S1, and S2.†

Deconvolution of each spectrum from 396 to 402 eV according to contributions from amino ($-NH_2$) and imine (C═N) nitrogens reveals a slight shift of amino fitted peaks to a higher binding energy by *ca.* 0.5 eV with increasing $Sc(OTf)_3$ concentration. Such a shift is expected upon coordination of the lone pair electron of the amino nitrogens with metals, as has been reported for Pd-imine COF coordination.[65] Here, the observed shift is attributed to the increasing amount of Sc $(OTf)_3$ coordinating with the N-containing dangling bonds associated with framework defects and/or the terminal edges of the COF framework, owing to the electron donation of lone

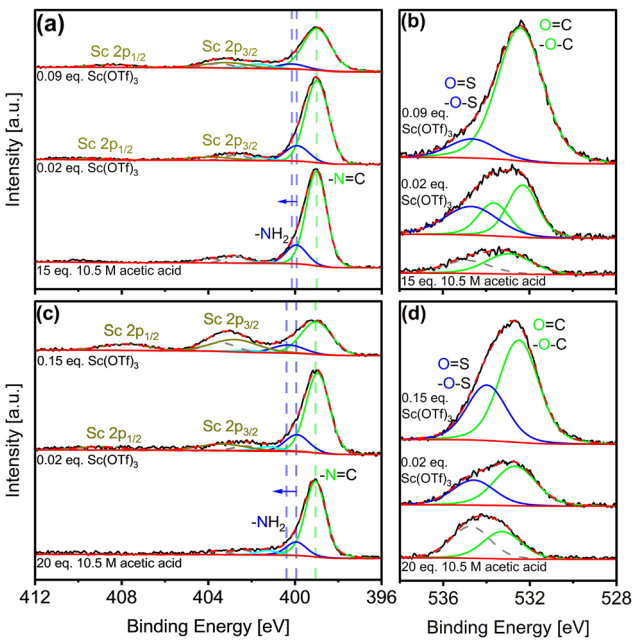

Fig. 3 XPS of as-made (a and b) COF-LZU1 and (c and d) TAPB-PDA synthesized under different catalytic conditions; (a and c) N 1s and Sc 2p spectra, (b and d) O 1s XPS spectra.

Table 1 XPS spectra-derived Sc to N ratio and O % (excluding O from $Sc(OTf)_3$) of as-made COF-LZU1 and TAPB-PDA synthesized under different catalytic conditions

	COF-LZU1		TAPB-PDA	
Catalytic condition	Sc : N	O % (pristine COFs)	Sc : N	O % (pristine COFs)
15 or 20 eq. 10.5 M acetic acid	N/A	2.74	N/A	5.40
0.02 eq. $Sc(OTf)_3$	0.03 : 1	3.79	0.05 : 1	3.45
0.09 eq. $Sc(OTf)_3$	0.07 : 1	11.59	—	—
0.15 eq. $Sc(OTf)_3$	—	—	0.16 : 1	9.27

pair electrons from amino nitrogens to Sc.[66] Additional quantification of O content (Fig. 3b and d) offers insight into framework formyl groups comprising defects and terminal dangling bonds. Specifically, the increase in oxygen content (Table 1) with increasing $Sc(OTf)_3$ catalyst concentration is indicative of commensurate increases of framework defects, likely resulting from the faster reaction kinetics during COF formation.[67,68]

Such defects are borne out by the COF crystallinity as revealed by comparison of experimental diffraction patterns collected from materials synthesized under specific catalytic conditions for nominal reaction times leading to the maximum crystallinity (Fig. S10†), with simulated XRD patterns (Fig. 4). Namely, the attenuation of XRD reflections with increasing $Sc(OTf)_3$ catalyst concentration is consistent with XPS evidence of concomitant increases in framework defects. Scherrer equation analysis of the (100) and (001) peaks reveals the presence of anisotropic crystallites with in-plane dimensions (*ca.* 21.7 nm) that average *ca.* 2.7–3 times the out-of-plane dimensions (Table S3†). Interlayer spacing, calculated from Bragg's law analysis of the (001) peak, was estimated to be *ca.* 3.5 Å under nearly all catalytic conditions considered.

Comparison of the 2θ angles of the (100) and (001) reflections as well as lattice parameters extracted from the Gaussian fittings of the peaks (Fig. S11†) and Pawley refinement of the diffraction patterns using Material Studio (Fig. S12†), confirms nearly eclipsed stacking in all cases.[47,63] A uniform shift of the reflections relative to the theoretical patterns for perfectly eclipsed structures is observed as the synthesis catalyst is changed between acetic acid and scandium triflate. The subtle shifts to lower angles in the case of the $Sc(OTf)_3$-catalyzed materials, indicate minor expansion of the unit cell that we attribute to sensitivity of the COF framework to metal coordination as reported in the literature.[69,70] The shifts to higher angles in the case of acetic acid-derived COFs indicate a relative contraction of the unit cell/pores. This reproducible phenomenona, one that we are investigating further, is likely a manifestation bond rotation owing to the weakening of π-π stacking energies upon shifting of COF layers under room temperature synthesis.

The emergence of subtle higher angle reflections in the case of TAPB-PDA synthesized under 0.09 eq. and higher $Sc(OTf)_3$ indicates the development of mixed crystalline phases.

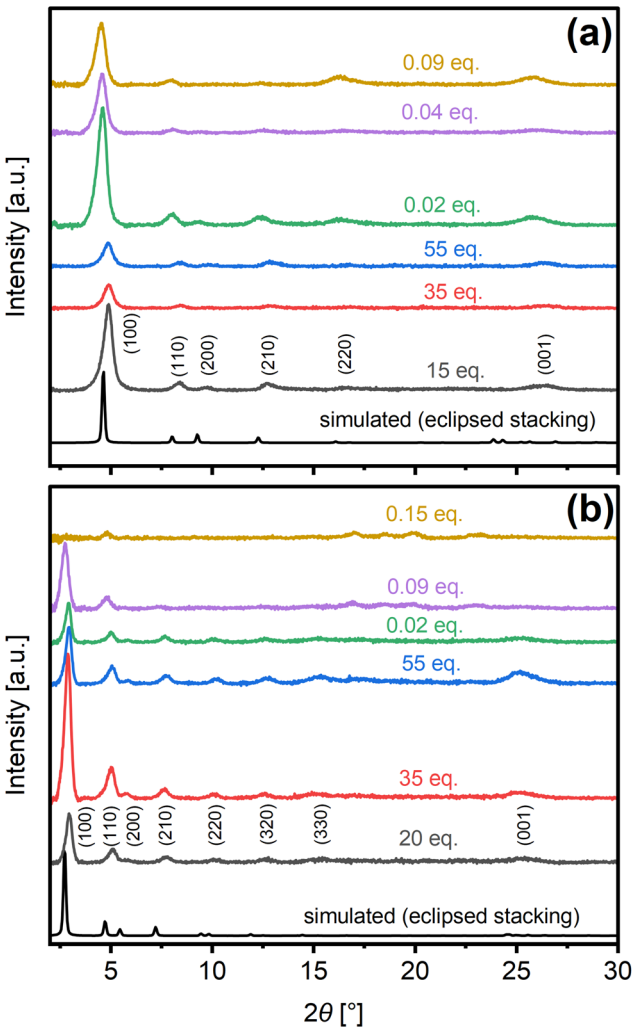

Fig. 4 Experimental PXRD patterns of as-made (a) COF-LZU1 and (b) TAPB-PDA synthesized under different catalytic conditions compared to patterns simulated for eclipsed structures.

Hence, we will focus on the apparently phase-pure COF-LZU1 for the remainder of this work.

DFT calculations: Sc(III) siting and mechanistic insight into anisotropic crystal growth

Motivated by the XPS evidence of $Sc(OTf)_3$ coordination with framework amines and imines (Fig. 3), we have carried out density functional theory (DFT) calculations to elucidate the strength of Sc(III) triflate coordination within the COF framework and to thereby assess where $Sc(OTf)_3$ is most likely to site. Specifically, as shown in Fig. 5, we have computed the binding energies associated with various $Sc(OTf)_3$-COF configurations enumerated in Fig. 2c, including the physical adsorption of $Sc(OTf)_3$ in the pores (Fig. 5a) and the coordination of $Sc(OTf)_3$ with various imine or amine functional groups, including coordination of $Sc(OTf)_3$ with an imine group of a pristine COF layer surface (*i.e.*, crystal 001 surface) (Fig. 5b), simultaneous coordination of $Sc(OTf)_3$ with an

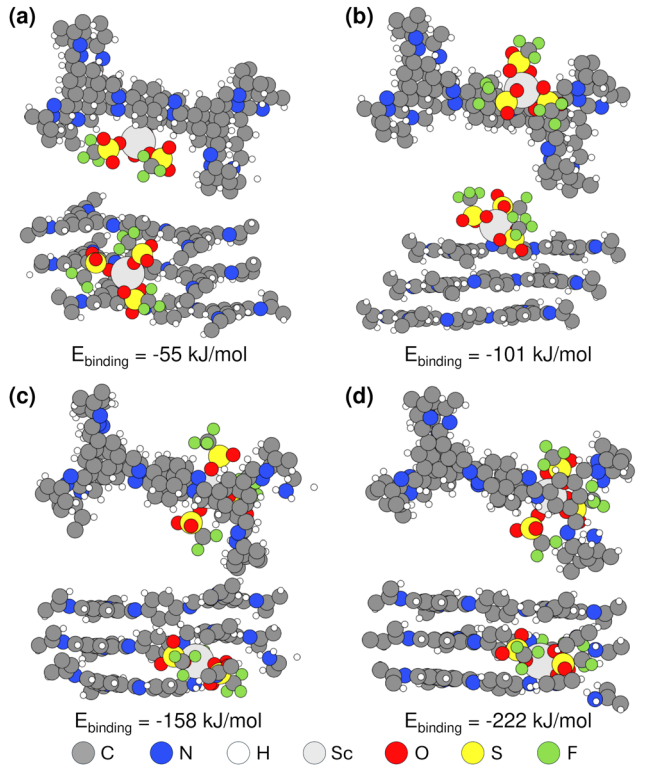

Fig. 5 DFT simulation results of optimized structures (top and side view) and the calculated binding energies within COF-LZU1 trilayers for $Sc(OTf)_3$ (a) physisorbed in the pore, (b) adsorbed on an imine bond of the top layer of the pristine COF-LZU1, (c) adsorbed on a single defect resulting in an imine-$Sc(OTf)_3$-amine linkage, and (d) coordinated with two defects resulting in an amine-$Sc(OTf)_3$-amine linkage.

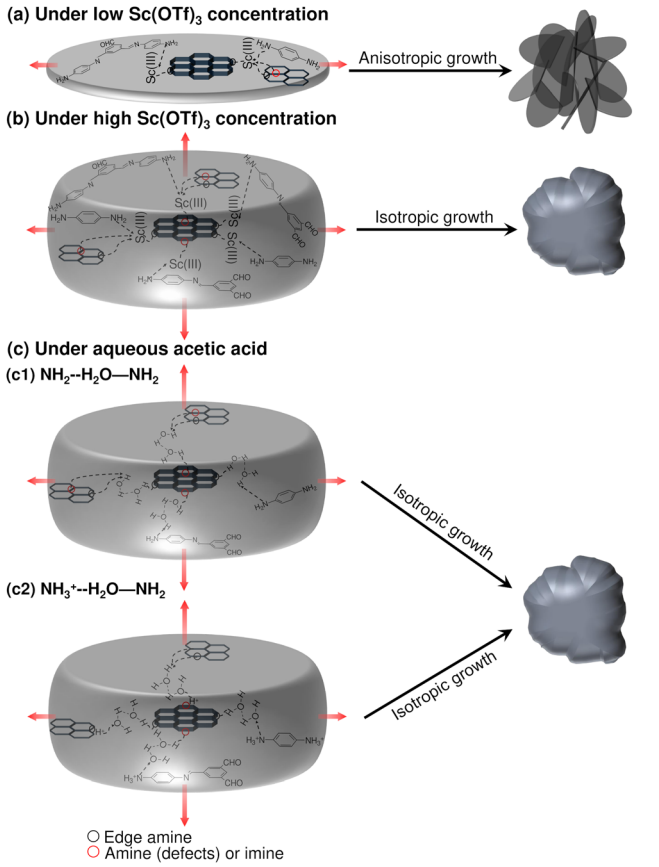

Scheme 2 Proposed mechanism of anisotropic and isotropic COF particle growth under different catalytic conditions.

amine comprising a framework defect and a framework imine within an adjacent COF layer (Fig. 5c), and co-coordination of $Sc(OTf)_3$ with amine groups comprising adjacent framework defects (Fig. 5d).

$Sc(OTf)_3$ coordinates most strongly to adjacent amines comprising a double framework defect, a configuration that is also representative of $Sc(OTf)_3$-mediated co-coordination between dangling amines terminating adjacent crystallites. This coordination state (BE: −222 kJ mol^{-1}) is 60–160 kJ mol^{-1} more favored than $Sc(OTf)_3$ coordinated with framework imines, and the strength of $Sc(OTf)_3$ binding with all frameork N exceeds by *ca.* 84–300% the energy associated with $Sc(OTf)_3$ physisorption in COF pores. The coordination of $Sc(OTf)_3$ with amino nitrogen rather than absorption in COF pores was confirmed by the shift of the amino fitted XPS peaks with increasing $Sc(OTf)_3$ concentrations (Fig. 3).

According to XPS analysis (Table S1†), amino nitrogen comprises at most *ca.* 15% of all N in the 0.02 eq. $Sc(OTf)_3$-catalyzed COF-LZU1, and terminal amines make up a maximum of *ca.* 8% of all N according to approximate crystallite sizes estimated from XRD data (Table S3 and Scheme S1†) in the limit of all terminal groups being amines and not formyl groups. Thus, the XPS-measured coordination of Sc with just 3% of all amino N in the case of 0.02 eq. $Sc(OTf)_3$-catalyzed COF-LZU1 (Table S1†), would be fully accomodated by terminal amines, the strongest and likely most accessible binding sites. Such preferential titration of terminal amines decorating the edge of 2D COF sheets at low $Sc(OTf)_3$ concentrations could enable recruitment of, and co-coordination with, amine-functionalized monomers, oligomers, or precursor sheets or nanocrystals at the edge of COF sheets (Scheme 2a). At the same time, the lack of $Sc(OTf)_3$ coordination with surface imines may suppress layer stacking and, thereby, result in anisotropic crystal growth consistent with the high-aspect-ratio features of the rosette structures formed at low $Sc(OTf)_3$ concentrations.

The relative binding energies determined by DFT calculations (Fig. 5) suggest that $Sc(OTf)_3$ would titrate amines/imines on the 2D COF layers only at higher concentrations of the catalyst. For the 0.09 eq. $Sc(OTf)_3$-catalyzed COF-LZU1, XPS analysis shows an increase in Sc coordination to 7% of all N (Table 1), likely exceeding the number of terminal amino N (Table S3 and Scheme S1†) when accounting for the inevitable mixture of amine and formyl group terminations, and thereby increasing the likelihood of $Sc(OTf)_3$ to also titrate more sterically hindered defect-derived framework amines and lower binding energy surface/framework imines. The concomitant coordinative bonding among amines/imines on different COF sheets supports the emergence of a sheet stacking mechanism

simultaneously with continued 2D COF sheet growth. Such isotropic growth is consistent with the observed formation of globular COF-LZU1 structures at higher $Sc(OTf)_3$ concentrations.

Complementary DFT calculations (Table S4†) show that the difference in binding energies between adjacent amine linkages and surface imines of *ca.* 120 kJ mol^{-1} is also preserved for other representative metal triflates (*e.g.*, Yb, Zn), suggesting that triflates may more generally preferentially titrate double framework defects and edge amines over surface imines. Yet, the higher binding energies for the Yb- and Zn-based triflates make it less clear whether sequential titration of these sites would similarly encourage preferential lateral layer growth or if the higher binding strengths may instead explain reports by Dichtel and co-workers[47] of the decreasing efficiency (Sc > Yb > Zn) of these catalysts to form crystalline 2D imine-based COF products.

When acetic acid is instead used as a catalyst, we conceive an isotropic growth mechanism like that which occurs at high $Sc(OTf)_3$ concentrations is at play in the formation of only globular structures. Namely, Jesus and Redinha[71] have demonstrated the hydrogen bonding of water with primary and/or protonated amines. Both types of amines likely populate COF framework edges and defects in this system, and hence serve as points for water- and/or acetic acid-mediated lateral growth of 2D COF layers and layer stacking as schematized in Scheme 2c. A third possibility for hydrogen bonding with amine radicals as reported in the literature,[72] is not considered here given the unlikely formation of amine radicals under the synthesis conditions studied.

We have determined (not shown) that 5 eq. of acetic acid is sufficient to drive COF-LZU1 formation, far exceeding the amount of catalyst equivalence in the case of $Sc(OTf)_3$-based COF-LZU1 synthesis (*i.e.*, 0.002–0.15 eq.). Therefore, the high concentrations of hydrogen bonding mediators (*i.e.*, acetic acid, water) under the minimal conditions sufficient for COF-LZU1 growth would enable simultaneous growth and stacking of COF layers akin to that observed for high concentrations of $Sc(OTf)_3$. Indeed, by introducing controlled amounts of water (as high as 60 eq.), and thereby more hydrogen bonding mediators, to 0.02 eq. $Sc(OTf)_3$ synthesis solutions, the COF-LZU1 morphology (Fig. S13†) evolves from its nominal rosette structure toward featureless globular structures bearing signature bonding and crystallinity as confirmed by FTIR (Fig. S14a†) and PXRD (Fig. S14b†), respectively.

Activation and textural analysis of a COF-LZU1

As-made COF-LZU1 products were activated by sequential solvent exhange. Initial methanol treatment removes residual solvents, as indicated by attenuation of FTIR bands at *ca.* 3000 cm^{-1} (dioxane, mesitylene) and 1617 cm^{-1} (mesitylene). Triflate ligands are also partially removed, as denoted by attenuation of peaks at 1660 cm^{-1}, *ca.* 1200–1300 cm^{-1}, and 1030 cm^{-1} (Fig. 6a). Low energy ion scattering (LEIS) (Fig. 6b) confirms clear attenuation of triflate-specific O, F, and S whereas the persistent Sc signal highlights the ineffectiveness of methanol for breaking coordination between Sc and framework N. Subsequent water washing is sufficient to break Sc–N coordination, leading to full removal of $Sc(OTf)_3$ as confirmed by the vanishing FTIR bands (*i.e.*, 1660 cm^{-1}, 1030 cm^{-1}) (Fig. 6a) and loss of F, S, and Sc LEIS signals (Fig. 6b). Powder XRD (Fig. 6c) and complementary SEM images (Fig. S15†) of activated COF-LZU1 samples synthesized under various catalytic conditions highlight the robustness of the crystallinity and morphology to full activation.

Nitrogen physisorption (Fig. 7) reveals Type 1(b) isotherms,[73] characterized by precipitous micropore filling that gives way, at higher relative pressures, to adsorption in distributed but narrow mesopores. Gradual multi-layer adsorption in mesostructures at intermediate relative pressures and unrestricted monolayer-to-multilayer adsorption at the highest relative pressures is most distinct in the case of the rosette material (0.02 eq. $Sc(OTf)_3$).

Cumulative surface areas, cumulative pore volumes, and corresponding quantitative textural measures (Table 2) derived from adsorption branch NLDFT analysis of triplicate COF syntheses help differentiate COF-LZU1 synthesized under the various catalytic conditions studied here. The globular acetic-

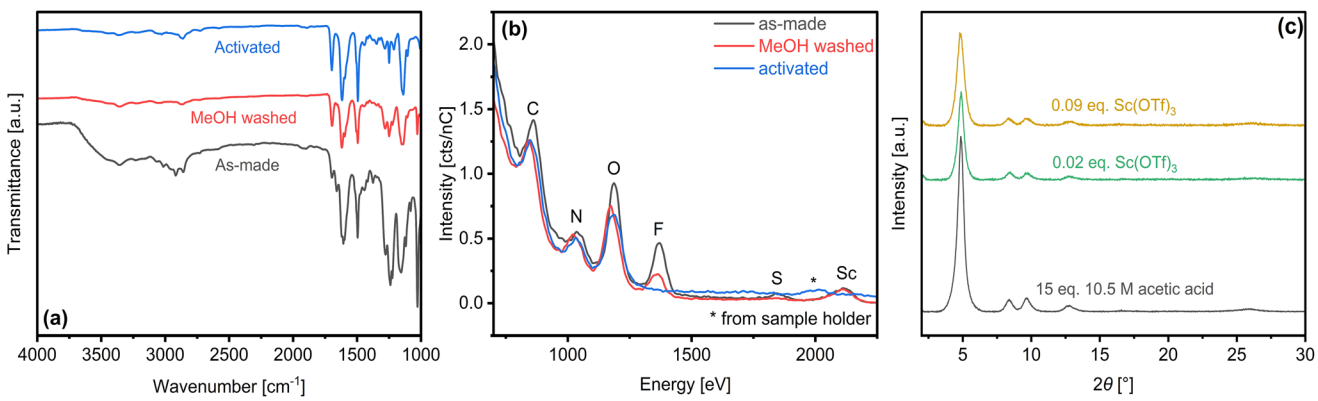

Fig. 6 (a) FTIR spectra and (b) average LEIS spectra over 3nm sputtering depth for 0.09 eq. $Sc(OTf)_3$-derived COF-LZU1 at points along the solvent activation process. (c) PXRD patterns of activated COF-LZU1 synthesized under different catalytic conditions.

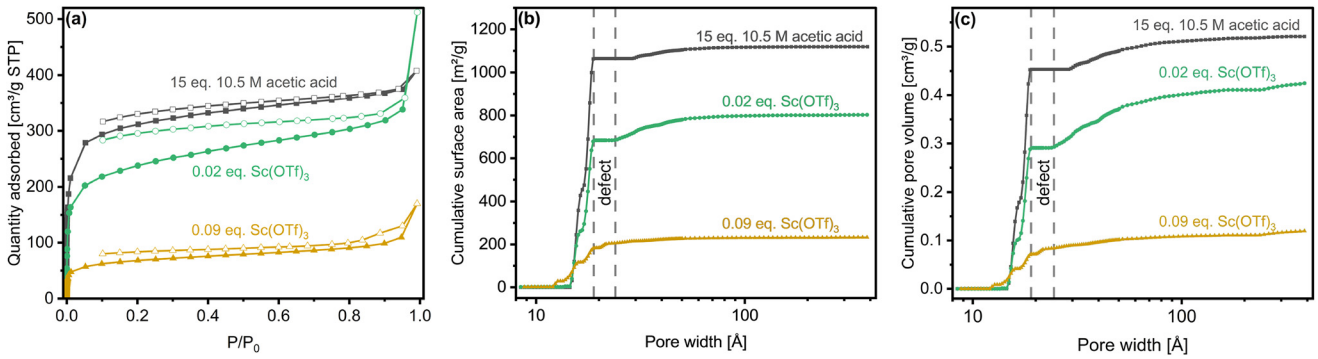

Fig. 7 Representative (a) N_2 adsorption and desorption isotherms (77K), (b) cumulative surface areas, and (c) cumulative pore volumes of activated COF-LZU1 synthesized under different catalytic conditions.

Table 2 Textural measures of activated COF-LZU1 synthesized under different catalytic conditions derived from N_2 adsorption isotherms at 77 K

Catalytic condition	S_{micro} [$m^2\ g^{-1}$]	S_{defect} [$m^2\ g^{-1}$]	$S_{external}$ [$m^2\ g^{-1}$]	S_{BET} [$m^2\ g^{-1}$]	V_{micro} [$cm^3\ g^{-1}$]	V_{defect} [$cm^3\ g^{-1}$]	$V_{external}$ [$cm^3\ g^{-1}$]	V_{total} [$cm^3\ g^{-1}$]
15 eq. 10.5 M acetic acid	1029 ± 44	0	52 ± 10	1149 ± 27	0.44 ± 0.01	0	0.06 ± 0.02	0.50 ± 0.02
0.02 eq. $Sc(OTf)_3$	782 ± 93	0	95 ± 21	906 ± 40	0.33 ± 0.04	0	0.11 ± 0.02	0.44 ± 0.02
0.09 eq. $Sc(OTf)_3$	163 ± 50	27 ± 3	30 ± 8	235 ± 40	0.06 ± 0.02	0.02 ± 0.01	0.05 ± 0.03	0.12 ± 0.003

acid synthesized material has the largest BET surface area (Table 2), attributable to its high crystallinity (Fig. 6c), whereas the total specific surface areas for the rosette and 0.09 eq. Sc $(OTf)_3$-synthesized globular structure were *ca.* 24% and 84% lower, respectively.

Micropore surface areas and pore volumes (Fig. 7b, c and Table 2), classically associated with pores of 20 Å or less in diameter, also trend with material crystallinity and defects. Namely, the most crystalline and least defective material prepared under acetic acid conditions shows the most crystalline micropores and, hence, the largest cumulative micropore surface area and micropore volume. The reduced crystallinity of the 0.02 eq. $Sc(OTf)_3$-derived material leads to *ca.* 25% reduction in both cumulative micropore surface area and micropore volume. The presence of significant framework defects, introduced when the highest amount (*i.e.*, 0.09 eq.) of $Sc(OTf)_3$ catalyst is used, further reduces the cumulative micropore surface area and micropore volume by *ca.* 82%. These defects are manifested by the corresponding distributions of features ('defect' in Fig. 7bc) in the *ca.* 19–23 Å size range that are absent in the case of the less-defected materials prepared with acetic acid and 0.02 eq. $Sc(OTf)_3$. The characteristic size of the defect features is consistent with the likely pore opening that occurs with framework defects (Fig. S16†). We estimate a corresponding surface area and pore volume associated with such defects in Table 2.

The general trends in textural measures change when it comes to external surface areas and pore volumes. Namely, the rosette materials (0.02 eq. $Sc(OTf)_3$) have the highest external surface area and pore volumes, nearly twice that of the acetic acid-derived materials and 2–3 times larger than the 0.09 eq. $Sc(OTf)_3$-derived materials. This stark difference in external textural measures can be simply rationalized according to the distinct hierarchical rosette morphology, and hence larger external surface area, of the 0.02 eq. $Sc(OTf)_3$-derived material.

Ultimately, the ability to realize hierarchically structured 2D COF-LZU1 with enhanced textural properties simply by multipurposing the $Sc(OTf)_3$ catalyst at room tempeature for 1 h, distinguishes this approach from others reported in the literature (Table S5†[41–46]) in terms of its simplicity, scalability, and sustainability. Specifically, alternative COF structuring strategies commonly introduce secondary templates (requiring separate synthesis) or growth modifiers, employ higher-temperature (sometimes solvothermal) conditions to achieve crystalline products, require extended reaction periods of up to 2–15 days, and rely on complicated, multi-step pre-, reaction, and post-processing conditions. Direct comparison of this work to literature reports of the impact of structuring on textural properties is confounded by differences in the specific COF frameworks reported. Yet, the *ca.* 286% enhancement of the BET surface area, achieved herein by structuring $Sc(OTf)_3$-catalyzed COF-LZU1 simply by reducing the catalyst concentration from 0.09 eq. (globular) to 0.02 eq. (rosette), is *ca.* 2–12 times higher than textural enhancements achieved in other COF systems.

Dye adsorption on activated COF-LZU1

In order to assess how the catalyst-tuned particle morphology and textural properties can be leveraged for applications, we have studied transient uptake and equilibrium adsorption of two cationic dyes, Rhodamine B (RdB) and Methylene blue (MB). These dyes were chosen on the basis of distinct kinetic diameters of *ca.* 11.3 Å and 5.1 Å, respectively, with RdB

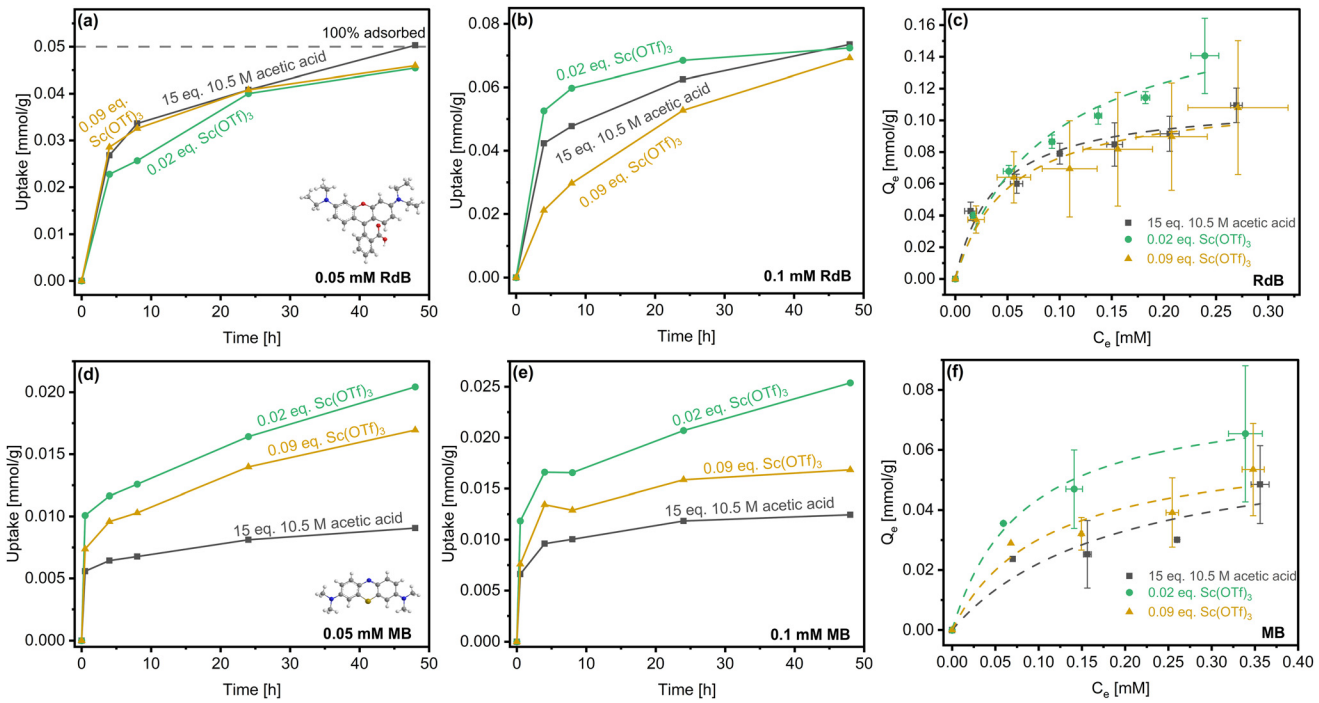

Fig. 8 Room temperature uptake from 0.05 mM and 0.1 mM (a and b) RdB and (d and e) MB solutions, and (c and f) corresponding adsorption isotherms (dashed lines represent Langmuir fits) for activated COF-LZU1 synthesized under different catalytic conditions.

approaching the characteristic pore size of COF-LZU1 (*ca.* 18 Å) and MB being significantly smaller.[13] In addition to van der Waals interactions of the dyes with the COF framework—specfiically in cases of strong confinement in the pores,[74] the positively charged N^+ and S^+ centers of RdB and MB, respectively, likely drive adsorption on the electron-rich imine and defect-derived amine sites within COFs (Fig. 8; equilibration times of 5 days (RdB) and 4 days (MB) established in Fig. S17†). Cationic dyes that were significantly smaller than (*e.g.*, 2-Naphthol, *ca.* 4–5 Å) and commensurate with (*e.g.*, Reactive Black 5, *ca.* 17.0 Å) the COF-LZU1 pore size were also studied, but both led to negligible uptake (not shown).

Fig. 8a and b show RdB uptake from solutions of two sorbate concentrations over a period of 48 h by representative COF-LZU1 prepared with acetic acid and $Sc(OTf)_3$ catalysts. In the case of the lower RdB concentration (0.05 mM, Fig. 8a), the uptake among the COF-LZU1 samples is effectively indistinguishable. Differentiation of the materials occurs at higher uptake, achieved upon doubling the RdB concentration (Fig. 8b). Specifically, the rate of uptake from 0.1 mM RdB solutions is fastest for the rosette-structured COF-LZU1 material (0.02 eq. $Sc(OTf)_3$) and slower for the globular particles, with the most sluggish uptake measured for the 0.09 eq. $Sc(OTf)_3$-derived material.

The sensitivity (or lack thereof) of the RdB uptake rates to adsorbents at the different sorbate concentrations can be understood in terms of the two modes of RdB adsorption on the accessible external surface and within the confining COF pores. While the textural properties vary among the three materials, the increasing rate of uptake at higher RdB concentrations (Fig. 8b) trends with increasing external surface area. Indeed, it is instructive to consider the maximum measured uptake relative to the estimated maximum loading of RdB that can be accomodated on the external surface of the three COF sorbents or directly within accesible pores, a measure we term $L_{max}|_{EXT}$ (Table 3).

Table 3 The maximum loading of dye that can be accomodated on the external surface of COF-LZU1 or directly within accesible pores ($L_{max}|_{EXT}$), affinities between dye and COF-LZU1 (K_L), and dye capacities of COF-LZU1 (Q_m)

	Rhodamine B			Methylene blue		
Catalytic condition of activated COF-LZU1	15 eq. 10.5 M acetic acid	0.02 eq. Sc $(OTf)_3$	0.09 eq. Sc $(OTf)_3$	15 eq. 10.5 M acetic acid	0.02 eq. Sc $(OTf)_3$	0.09 eq. Sc $(OTf)_3$
$L_{max}\|_{EXT}$ [mmol g^{-1}]	0.06 ± 0.01	0.12 ± 0.03	0.04 ± 0.01	0.12 ± 0.03	0.25 ± 0.06	0.08 ± 0.02
K_L [M^{-1}]	2.6×10^4	1.2×10^4	1.9×10^4	5.2×10^3	1.2×10^4	9.3×10^3
Q_m [mmol g^{-1}]	0.11	0.18	0.12	0.06	0.08	0.06

In the case of the lower RdB concentrations (Fig. 8a), the maximum specific uptake of *ca.* 0.045 mmol g^{-1} (48 h) can be nearly completely accommodated by adsorption on the accessible external surfaces of the three sorbents or directly within accessible pores without the slower diffusion into the COF pores impacting the uptake. Increasing the RdB concentration (Fig. 8b), however, results in higher RdB uptake (*ca.* 0.07 mmol g^{-1} at 48 h) that reaches or exceeds $L_{max}|_{EXT}$ of the acetic acid- and 0.09 eq. $Sc(OTf)_3$-synthesized materials, respectively. Specifically, with the lowest external surface area and hence fewest directly accessible COF pores, uptake by the 0.09 eq. $Sc(OTf)_3$-synthesized sorbent is the first to be noticeably impacted by the sluggish rate-limiting diffusion of RdB in the COF pores. With further uptake, $L_{max}|_{EXT}$ of the acetic acid-synthesized material is approached next, such that restricted RdB adsorption and diffusion in the associated COF pores slows the overall uptake. Ultimately, the total uptake is only approximately half the $L_{max}|_{EXT}$ of the rosette-structured 0.02 eq. $Sc(OTf)_3$-synthesized sorbent, with the most rapid RdB uptake resulting from adsorption on the accessible rosette surfaces and directly in accessible pores minimizing the impact of the slower diffusion in COF pores.

The impact of the accessible external surface area and thereby directly accessible pores of the rosette-structured sorbent over the globular sorbents is further indicated by the RdB isotherms collected at room temperature for the three materials (Fig. 8c). Langmuir fitting of the isotherms enabled calculations of the affinities (K_L) and capacities (Q_m) of dyes for the various activated COF-LZU1 samples (Table 3). The equilibrium isotherms are statistically indistinguishable at low RdB concentrations below the $L_{max}|_{EXT}$, and remain indistinguishable for the two globular materials even at higher sorbate concentrations despite the nearly sixfold higher total specific surface area of the acetic acid-derived COF-LZU1 relative to the 0.09 eq. $Sc(OTf)_3$-synthesized material (Table 2). We hypothesize that the lower total specific surface area of the latter is offset by the larger number of framework defects (Table 1) comprising electron-rich terminal amines that serve as strong binding sites for RdB *via* its positively charged N^+ center. Strong dispersion forces likely also contribute, in part, to this common equilibrium adsorption.

We attribute the divergence of the isotherm measured for the rosette sample at higher RdB concentrations to the contributions of enhanced sites for adsorption on the higher accessible external surface area. Such surface-dominated adsorption, for which dispersion forces are commonly weaker than for molecules under pore confinment, is further supported by the lower effective affinity, K_L, for RdB on the rosette-structured materials compared to globular materials where we expect pore adsorption to play a bigger role at equilibrium.

Uptake of the smaller MB molecule (Fig. 8d and e) falls well below the $L_{max}|_{EXT}$ (Table 3) for all three materials at both sorbate concentrations studied. Hence, the total uptake should be accomodated in all cases by adsorption on the external surface or directly in the accessible COF pores. The much smaller size of MB relative to the COF-LZU1 pore size likely limits the role of dispersion forces in MB adsorption and certainly eliminates any possible impact of diffusion limits on uptake. Instead, interaction of the S^+ center of MB with electron-rich imine and defect-derived amine sites within COFs is expected to dominate adsorption, such that the differences in the uptake rates and equilibrium adsorption capacity can be attributed to differences in the number of accessible adsorption sites in these materials.

The most sluggish uptake and lowest equilibrium adsorption capacity occurs over the globular acetic acid-derived sample, owing to it being the least defective material. The larger number of defects (Table 1) in the 0.09 eq. $Sc(OTf)_3$-catalyzed materials result in more rapid uptake, higher affinity, and similar capacity (Fig. 8f). The most rapid uptake and highest MB capacity are measured for the rosette-structured material (Fig. 8d–f and Table 3). While the specific defects are lower in this material than in the globular 0.09 eq. $Sc(OTf)_3$-synthesized sample (Table 1), the hierarchical structure of the material (*i.e.*, its *ca.* 4.5-fold higher external surface area) likely offers access to a larger specific number of those defects, resulting in the highest MB adsorption capacity.

Conclusions

The identification of facile strategies for tailoring structural hierarchy of porous materials is key to accessing diffusion length scales suitable for the efficient manipulation of molecules and ease of processing required for applications. Here, we have identified how catalytic conditions alone can be exploited as a powerful and scalable handle for tuning morphology of 2D imine-based COFs without the need to introduce complex structuring strategies, employ higher temperatures, require extended reaction periods, or rely on complicated multi-step reaction and processing steps. Through combined experimental and computational insights, this work offers mechanistic insight into the dual role of $Sc(OTf)_3$ as an efficient synthetic catalyst and growth modifier. Rather than optimizing the system to minimize crystalline defects, we show how the titration of framework defects and terminal groups of different binding strengths can instead be exploited to tune crystal growth. The result is the ability to switch from isotropic crystal growth of globular porous materials with large diffusion length scales to anisotropic crystal growth of interconnected high-aspect-ratio hierarchical products. The sensitivity of this mechanism to triflate binding strength (*e.g.*, stronger binding calculated for alternative metal triflates) and the influence of synthesis temperature (*e.g.*, solvothermal processing) and pore topology (*e.g.*, non-hexagonal topologies including triangular, rhombic, square, pentagonal) on the resulting morphology remain as potential additional design handles to be explored in the future. Yet, the rosette-structured COFs in this work offer unique textural properties with dramatically enhanced external surface area, highly accessible pores, and reduced diffusion length scales enabling their efficient interaction with bulky molecular sorbates. More generally, by exploiting rather than eliminating framework defects, this work offers a unique strategy for morphological design and COF synthesis

that should extend beyond sorbents to impact anisotropic growth of COF thin films as a means for extending its impact.

Author contributions

Hao Guo: investigation, methodology, and writing. Joseph P. Cline: formal analysis and reviewing. Ryan Thorpe: formal analysis and reviewing. Christopher J. Kiely: validation, writing, and reviewing. Srinivas Rangarajan: funding acquisition, formal analysis, methodology, visualization, writing, and reviewing. Mark A. Snyder: conceptualization, funding acquisition, methodology, project administration, supervision, validation, visualization, writing, and reviewing.

Data availability

The data supporting this article have been included as part of the ESI.†

Conflicts of interest

There are no conflicts to declare.

Acknowledgements

The authors gratefully acknowledge support for this work from the National Science Foundation, through the grant number CBET-1953245, and *via* a grant from the Commonwealth of Pennsylvania, Department of Community and Economic Development, through the Pennsylvania Infrastructure Technology Alliance (PITA). Portions of this research were conducted on Lehigh University's Research Computing infrastructure partially supported by NSF Award OAC-2019035. In addition, the authors gratefully acknowledge access to the Lehigh University Institute for Functional Materials and Devices Materials Characterization Facility (MCF).

References

1 A. P. Côté, H. M. El-Kaderi, H. Furukawa, J. R. Hunt and O. M. Yaghi, Reticular Synthesis of Microporous and Mesoporous 2D Covalent Organic Frameworks, *J. Am. Chem. Soc.*, 2007, **129**(43), 12914–12915, DOI: **10.1021/ja0751781**.

2 H. M. El-Kaderi, J. R. Hunt, J. L. Mendoza-Cortés, A. P. Côté, R. E. Taylor, M. O'Keeffe and O. M. Yaghi, Designed Synthesis of 3D Covalent Frameworks, *Science*, 2007, **316**(5822), 268–272, DOI: **10.1126/science.1139055**.

3 N. Huang, P. Wang and D. Jiang, Covalent Organic Frameworks: A Materials Platform for Structural and Functional Designs, *Nat. Rev. Mater.*, 2016, **1**, 16068, DOI: **10.1038/natrevmats.2016.68**.

4 X. Li, S. Cai, B. Sun, C. Yang, J. Zhang and Y. Liu, Chemically Robust Covalent Organic Frameworks: Progress and Perspective, *Matter*, 2020, **3**(5), 1507–1540, DOI: **10.1016/j.matt.2020.09.007**.

5 L. Cusin, H. Peng, A. Ciesielski and P. Samorì, Chemical Conversion and Locking of the Imine Linkage: Enhancing the Functionality of Covalent Organic Frameworks, *Angew. Chem., Int. Ed.*, 2021, **60**(26), 14236–14250, DOI: **10.1002/anie.202016667**.

6 Y. Yusran, X. Guan, H. Li, Q. Fang and S. Qiu, Postsynthetic Functionalization of Covalent Organic Frameworks, *Natl. Sci. Rev.*, 2020, **7**(1), 170–190, DOI: **10.1093/nsr/nwz122**.

7 C. S. Diercks and O. M. Yaghi, The Atom, the Molecule, and the Covalent Organic Framework, *Science*, 2017, **355**(6328), eaal1585, DOI: **10.1126/science.aal1585**.

8 W. Ji, L. Xiao, Y. Ling, C. Ching, M. Matsumoto, R. P. Bisbey, D. E. Helbling and W. R. Dichtel, Removal of GenX and Perfluorinated Alkyl Substances from Water by Amine-Functionalized Covalent Organic Frameworks, *J. Am. Chem. Soc.*, 2018, **140**(40), 12677–12681, DOI: **10.1021/jacs.8b06958**.

9 Y. Peng, Z. Hu, Y. Gao, D. Yuan, Z. Kang, Y. Qian, N. Yan and D. Zhao, Synthesis of a Sulfonated Two-Dimensional Covalent Organic Framework as an Efficient Solid Acid Catalyst for Biobased Chemical Conversion, *ChemSusChem*, 2015, **8**(19), 3208–3212, DOI: **10.1002/cssc.201500755**.

10 H. Fan, M. Peng, I. Strauss, A. Mundstock, H. Meng and J. Caro, High-Flux Vertically Aligned 2D Covalent Organic Framework Membrane with Enhanced Hydrogen Separation, *J. Am. Chem. Soc.*, 2020, **142**(15), 6872–6877, DOI: **10.1021/jacs.0c00927**.

11 Y. J. Hou, J. Deng, K. He, C. Chen and Y. Yang, Covalent Organic Frameworks-Based Solid-Phase Microextraction Probe for Rapid and Ultrasensitive Analysis of Trace Per- A Nd Polyfluoroalkyl Substances Using Mass Spectrometry, *Anal. Chem.*, 2020, **92**(15), 10213–10217, DOI: **10.1021/acs.analchem.0c01829**.

12 A. G. Slater and A. I. Cooper, Function-Led Design of New Porous Materials, *Science*, 2015, **348**(6238), aaa8075, DOI: **10.1126/science.aaa8075**.

13 H. Wang, Y. Yang, X. Yuan, W. L. Teo, Y. Wu, L. Tang and Y. Zhao, Structure–Performance Correlation Guided Applications of Covalent Organic Frameworks, *Mater. Today*, 2022, **53**, 106–133, DOI: **10.1016/j.mattod.2022.02.001**.

14 Y. Tang, W. Li, Y. Muhammad, S. Jiang, M. Huang, H. Zhang, Z. Zhao and Z. Zhao, Fabrication of Hollow Covalent-Organic Framework Microspheres via Emulsion-Interfacial Strategy to Enhance Laccase Immobilization for Tetracycline Degradation, *Chem. Eng. J.*, 2021, **421**, 129743, DOI: **10.1016/j.cej.2021.129743**.

15 S. Karak, K. Dey and R. Banerjee, Maneuvering Applications of Covalent Organic Frameworks via Framework-Morphology Modulation, *Adv. Mater.*, 2022, **34**(49), 2202751, DOI: **10.1002/adma.202202751**.

16 D. P. Serrano, J. M. Escola and P. Pizarro, Synthesis Strategies in the Search for Hierarchical Zeolites, *Chem.*

Soc. Rev., 2013, **42**(9), 4004–4035, DOI: **10.1039/C2CS35330J**.

17 A. Primo and H. Garcia, Zeolites as Catalysts in Oil Refining, *Chem. Soc. Rev.*, 2014, **43**, 7548–7561, DOI: **10.1039/c3cs60394f**.

18 A. Corma, Inorganic Solid Acids and Their Use in Acid-Catalyzed Hydrocarbon Reactions, *Chem. Rev.*, 1995, **95**(3), 559–614, DOI: **10.1021/cr00035a006**.

19 L. H. Chen, M. H. Sun, Z. Wang, W. Yang, Z. Xie and B. L. Su, Hierarchically Structured Zeolites: From Design to Application, *Chem. Rev.*, 2020, **120**(20), 11194–11294, DOI: **10.1021/acs.chemrev.0c00016**.

20 W. Fan, M. A. Snyder, S. Kumar, P.-S. Lee, W. C. Yoo, A. V. McCormick, R. L. Penn, A. Stein and M. Tsapatsis, Hierarchical Nanofabrication of Microporous Crystals with Ordered Mesoporosity, *Nat. Mater.*, 2008, **7**(12), 984–991, DOI: **10.1038/nmat2302**.

21 H. Chen, J. Wydra, X. Zhang, P.-S. Lee, Z. Wang, W. Fan and M. Tsapatsis, Hydrothermal Synthesis of Zeolites with Three-Dimensionally Ordered Mesoporous-Imprinted Structure, *J. Am. Chem. Soc.*, 2011, **133**(32), 12390–12393, DOI: **10.1021/ja2046815**.

22 M. Choi, K. Na, J. Kim, Y. Sakamoto, O. Terasaki and R. Ryoo, Stable Single-Unit-Cell Nanosheets of Zeolite MFI as Active and Long-Lived Catalysts, *Nature*, 2009, **461**(7261), 246–249, DOI: **10.1038/nature08288**.

23 D. Xu, Y. Ma, Z. Jing, L. Han, B. Singh, J. Feng, X. Shen, F. Cao, P. Oleynikov, H. Sun, O. Terasaki and S. Che, π-π Interaction of Aromatic Groups in Amphiphilic Molecules Directing for Single-Crystalline Mesostructured Zeolite Nanosheets, *Nat. Commun.*, 2014, **5**, 4262, DOI: **10.1038/ncomms5262**.

24 K. Na, C. Jo, J. Kim, K. Cho, J. Jung, Y. Seo, R. J. Messinger, B. F. Chmelka and R. Ryoo, Directing Zeolite Structures into Hierarchically Nanoporous Architectures, *Science*, 2011, **333**, 328–332, DOI: **10.1126/science.1205785**.

25 D. Xu, G. R. Swindlehurst, H. Wu, D. H. Olson, X. Zhang and M. Tsapatsis, On the Synthesis and Adsorption Properties of Single-Unit-Cell Hierarchical Zeolites Made by Rotational Intergrowths, *Adv. Funct. Mater.*, 2014, **24**(2), 201–208, DOI: **10.1002/adfm.201301975**.

26 X. Zhang, D. Liu, D. Xu, S. Asahina, K. A. Cychosz, K. V. Agrawal, Y. Al Wahedi, A. Bhan, S. Al Hashimi, O. Terasaki, M. Thommes and M. Tsapatsis, Synthesis of Self-Pillared Zeolite Nanosheets by Repetitive Branching, *Science*, 2012, 336((6089)), 1684–1687. DOI: **10.1126/science.1221111**.

27 S. T. Emmerling, R. Schuldt, S. Bette, L. Yao, R. E. Dinnebier, J. Kästner and B. V. Lotsch, Interlayer Interactions as Design Tool for Large-Pore COFs, *J. Am. Chem. Soc.*, 2021, **143**(38), 15711–15722, DOI: **10.1021/jacs.1c06518**.

28 Z. Qu, C. Lai, G. Zhao, A. Knebel, H. Fan and H. Meng, Pore Engineering in Covalent Organic Framework Membrane for Gas Separation, *Adv. Membr.*, 2022, **2**, 100037, DOI: **10.1016/j.advmem.2022.100037**.

29 K. Geng, T. He, R. Liu, S. Dalapati, K. T. Tan, Z. Li, S. Tao, Y. Gong, Q. Jiang and D. Jiang, Covalent Organic Frameworks: Design, Synthesis, and Functions, *Chem. Rev.*, 2020, **120**(16), 8814–8933, DOI: **10.1021/acs.chemrev.9b00550**.

30 T. Sick, J. M. Rotter, S. Reuter, S. Kandambeth, N. N. Bach, M. Döblinger, J. Merz, T. Clark, T. B. Marder, T. Bein and D. D. Medina, Switching on and off Interlayer Correlations and Porosity in 2D Covalent Organic Frameworks, *J. Am. Chem. Soc.*, 2019, **141**(32), 12570–12581, DOI: **10.1021/jacs.9b02800**.

31 A. M. Pütz, M. W. Terban, S. Bette, F. Haase, R. E. Dinnebier and B. V. Lotsch, Total Scattering Reveals the Hidden Stacking Disorder in a 2D Covalent Organic Framework, *Chem. Sci.*, 2020, **11**(47), 12647–12654, DOI: **10.1039/d0sc03048a**.

32 W. Wang, Y. Jia, S. Zhou and S. Deng, Removal of Typical PFAS from Water by Covalent Organic Frameworks with Different Pore Sizes, *J. Hazard. Mater.*, 2023, **460**, 132522, DOI: **10.1016/j.jhazmat.2023.132522**.

33 N. Zhang, A. Ishag, Y. Li, H. Wang, H. Guo, P. Mei, Q. Meng and Y. Sun, Recent Investigations and Progress in Environmental Remediation by Using Covalent Organic Framework-Based Adsorption Method: A Review, *J. Cleaner Prod.*, 2020, **277**, 123360, DOI: **10.1016/j.jclepro.2020.123360**.

34 X. Liu, H. Pang, X. Liu, Q. Li, N. Zhang, L. Mao, M. Qiu, B. Hu, H. Yang and X. Wang, Orderly Porous Covalent Organic Frameworks-Based Materials: Superior Adsorbents for Pollutants Removal from Aqueous Solutions, *Innovation*, 2021, **2**(1), 100076, DOI: **10.1016/j.xinn.2021.100076**.

35 V. D. da Silva, K. Zalewska, Z. Petrovski, C. D. Buarque, L. C. Branco and P. M. Esteves, Covalent Organic Frameworks as Promising Materials for the Removal of Metal and Organic Pollutants from Water, *Mater. Today Sustainability*, 2023, **270**, 129523, DOI: **10.1016/j.mtsust.2022.100279**.

36 A. R. Bagheri, N. Aramesh, F. Sher and M. Bilal, Covalent Organic Frameworks as Robust Materials for Mitigation of Environmental Pollutants, *Chemosphere*, 2021, **270**, 129523, DOI: **10.1016/j.chemosphere.2020.129523**.

37 L. Yang, L. Shao, Z. Wu, P. Zhan and L. Zhang, Design and Synthesis of Porous Organic Polymers: Promising Catalysts for Lignocellulose Conversion to 5-Hydroxymethylfurfural and Derivates, *Polymers*, 2023, **15**(12), 2630, DOI: **10.3390/polym15122630**.

38 C. H. Feriante, S. Jhulki, A. M. Evans, R. R. Dasari, K. Slicker, W. R. Dichtel and S. R. Marder, Rapid Synthesis of High Surface Area Imine-Linked 2D Covalent Organic Frameworks by Avoiding Pore Collapse During Isolation, *Adv. Mater.*, 2020, **32**(2), 1905776, DOI: **10.1002/adma.201905776**.

39 M. Xue, J. Yang, F. Kang, X. Wang and Q. Zhang, Recent Progress in Single-Crystal Structures of Organic Polymers, *J. Mater. Chem. C*, 2022, **10**, 17027–17047, DOI: **10.1039/d2tc02170f**.

40 X. Wang, Z. Mu, P. Shao and X. Feng, Hierarchically Porous Covalent Organic Frameworks: Synthesis Methods and Applications, *Chem. – Eur. J.*, 2024, **30**(14), e202303601, DOI: **10.1002/chem.202303601**.

41 B. Garai, D. Shetty, T. Skorjanc, F. Gándara, N. Naleem, S. Varghese, S. K. Sharma, M. Baias, R. Jagannathan, M. A. Olson, S. Kirmizialtin and A. Trabolsi, Taming the Topology of Calix[4]Arene-Based 2D-Covalent Organic Frameworks: Interpenetrated vs Noninterpenetrated Frameworks and Their Selective Removal of Cationic Dyes, *J. Am. Chem. Soc.*, 2021, **143**(9), 3407–3415, DOI: **10.1021/jacs.0c12125**.

42 S. Karak, K. Dey, A. Torris, A. Halder, S. Bera, F. Kanheerampockil and R. Banerjee, Inducing Disorder in Order: Hierarchically Porous Covalent Organic Framework Nanostructures for Rapid Removal of Persistent Organic Pollutants, *J. Am. Chem. Soc.*, 2019, **141**(18), 7572–7581, DOI: **10.1021/jacs.9b02706**.

43 W. Li, H. X. Jiang, M. F. Cui, R. Wang, A. N. Tang and D. M. Kong, SiO_2 Templates-Derived Hierarchical Porous COFs Sample Pretreatment Tool for Non-Targeted Analysis of Chemicals in Foods, *J. Hazard. Mater.*, 2022, **432**, 128705, DOI: **10.1016/j.jhazmat.2022.128705**.

44 X. Zhao, P. Pachfule, S. Li, T. Langenhahn, M. Ye, C. Schlesiger, S. Praetz, J. Schmidt and A. Thomas, Macro/Microporous Covalent Organic Frameworks for Efficient Electrocatalysis, *J. Am. Chem. Soc.*, 2019, **141**(16), 6623–6630, DOI: **10.1021/jacs.9b01226**.

45 Z. Mu, Y. Zhu, Y. Zhang, A. Dong, C. Xing, Z. Niu, B. Wang and X. Feng, Hierarchical Microtubular Covalent Organic Frameworks Achieved by COF-to-COF Transformation, *Angew. Chem., Int. Ed.*, 2023, **62**(17), e202300373, DOI: **10.1002/anie.202300373**.

46 S. Wang, Y. Yang, H. Zhang, Z. Zhang, C. Zhang, X. Huang, D. Kozawa, P. Liu, B. G. Li and W. J. Wang, Toward Covalent Organic Framework Metastructures, *J. Am. Chem. Soc.*, 2021, **143**(13), 5003–5010, DOI: **10.1021/jacs.0c13090**.

47 M. Matsumoto, R. R. Dasari, W. Ji, C. H. Feriante, T. C. Parker, S. R. Marder and W. R. Dichtel, Rapid Low Temperature Formation of Imine-Linked Covalent Organic Frameworks Catalyzed by Metal Triflates, *J. Am. Chem. Soc.*, 2017, **139**(14), 4999–5002, DOI: **10.1021/jacs.7b01240**.

48 C. Feriante, A. M. Evans, S. Jhulki, I. Castano, M. J. Strauss, S. Barlow, W. R. Dichtel and S. R. Marder, New Mechanistic Insights into the Formation of Imine-Linked Two-Dimensional Covalent Organic Frameworks, *J. Am. Chem. Soc.*, 2020, **142**(43), 18637–18644, DOI: **10.1021/jacs.0c08390**.

49 B. J. Smith, A. C. Overholts, N. Hwang and W. R. Dichtel, Insight into the Crystallization of Amorphous Imine-Linked Polymer Networks to 2D Covalent Organic Frameworks, *Chem. Commun.*, 2016, **52**(18), 3690–3693, DOI: **10.1039/c5cc10221a**.

50 S. Wang, V. A. Reddy, M. C. Y. Ang, J. Cui, D. T. Khong, Y. Han, S. I. Loh, R. Cheerlavancha, G. P. Singh, S. Rajani and M. S. Strano, Single-Crystal 2D Covalent Organic Frameworks for Plant Biotechnology, *J. Am. Chem. Soc.*, 2023, **145**(22), 12155–12163, DOI: **10.1021/jacs.3c01783**.

51 D. Ongari, A. V. Yakutovich, L. Talirz and B. Smit, Building a Consistent and Reproducible Database for Adsorption Evaluation in Covalent-Organic Frameworks, *ACS Cent. Sci.*, 2019, **5**(10), 1663–1675, DOI: **10.1021/acscentsci.9b00619**.

52 G. Kresse and J. Furthmüller, *Efficiency of Ab initio Total Energy Calculations for Metals and Semiconductors Using a Plane-Wave Basis Set*, 1996, vol. 6.

53 J. P. Perdew, K. Burke and M. Ernzerhof, *Generalized Gradient Approximation Made Simple*, 1996.

54 S. Grimme, Accurate Description of van Der Waals Complexes by Density Functional Theory Including Empirical Corrections, *J. Comput. Chem.*, 2004, **25**(12), 1463–1473, DOI: **10.1002/jcc.20078**.

55 S. Grimme, Semiempirical GGA-Type Density Functional Constructed with a Long-Range Dispersion Correction, *J. Comput. Chem.*, 2006, **27**(15), 1787–1799, DOI: **10.1002/jcc.20495**.

56 S. Grimme, J. Antony, S. Ehrlich and H. Krieg, A Consistent and Accurate Ab Initio Parametrization of Density Functional Dispersion Correction (DFT-D) for the 94 Elements H-Pu, *J. Chem. Phys.*, 2010, **132**(15), 154104, DOI: **10.1063/1.3382344**.

57 W. Chen, P. Chen, D. Chen, Y. Liu, G. Zhang, L. Wang and L. Chen, Triangular Topological 2D Covalent Organic Frameworks Constructed via Symmetric or Asymmetric "Two-in-One" Type Monomers, *Adv. Sci.*, 2022, **9**(19), 2105517, DOI: **10.1002/advs.202105517**.

58 A. Natraj, W. Ji, J. Xin, I. Castano, D. W. Burke, A. M. Evans, M. J. Strauss, M. Ateia, L. S. Hamachi, N. C. Gianneschi, Z. A. Alothman, J. Sun, K. Yusuf and W. R. Dichtel, Single-Crystalline Imine-Linked Two-Dimensional Covalent Organic Frameworks Separate Benzene and Cyclohexane Efficiently, *J. Am. Chem. Soc.*, 2022, **144**(43), 6366–6378, DOI: **10.1021/jacs.2c07166**.

59 C. Xiong, H. Ning, G. Jia, X. Hong, X. Fei and J. Donglin, Towards Covalent Organic Frameworks with Predesignable and Aligned Open Docking Sites, *Chem. Commun.*, 2014, **50**(46), 6161–6163, DOI: **10.1039/c4cc01825g**.

60 F. Wen, K. Xu, Y. Feng and N. Huang, Two-Dimensional Covalent Organic Frameworks with Pentagonal Pores, *J. Am. Chem. Soc.*, 2024, **146**(29), 19680–19685, DOI: **10.1021/jacs.4c06438**.

61 T. Banerjee, F. Haase, S. Trenker, B. P. Biswal, G. Savasci, V. Duppel, I. Moudrakovski, C. Ochsenfeld and B. V. Lotsch, Sub-Stoichiometric 2D Covalent Organic Frameworks from Tri- and Tetratopic Linkers, *Nat. Commun.*, 2019, **10**(1), 2689, DOI: **10.1038/s41467-019-10574-6**.

62 S. Y. Ding, X. H. Cui, J. Feng, G. Lu and W. Wang, Facile Synthesis of -C=N- Linked Covalent Organic Frameworks under Ambient Conditions, *Chem. Commun.*, 2017, **53**(87), 11956–11959, DOI: **10.1039/c7cc05779b**.

63 S. Y. Ding, J. Gao, Q. Wang, Y. Zhang, W. G. Song, C. Y. Su and W. Wang, Construction of Covalent Organic

Framework for Catalysis: Pd/COF-LZU1 in Suzuki-Miyaura Coupling Reaction, *J. Am. Chem. Soc.*, 2011, **133**(49), 19816–19822, DOI: **10.1021/ja206846p**.

64 Y. He, N. An, C. Meng, K. Xie, X. Wang, X. Dong, D. Sun, Y. Yang and Z. Hu, High-Density Active Site COFs with a Flower-like Morphology for Energy Storage Applications, *J. Mater. Chem. A*, 2022, **10**, 11030–11038, DOI: **10.1039/D2TA01065H**.

65 I. Romero-Muñiz, A. Mavrandonakis, P. Albacete, A. Vega, V. Briois, F. Zamora and A. E. Platero-Prats, Unveiling the Local Structure of Palladium Loaded into Imine-Linked Layered Covalent Organic Frameworks for Cross-Coupling Catalysis, *Angew. Chem., Int. Ed.*, 2020, **59**(31), 13013–13020, DOI: **10.1002/anie.202004197**.

66 L. Wang, H. Xu, Y. Qiu, X. Liu, W. Huang, N. Yan and Z. Qu, Utilization of Ag Nanoparticles Anchored in Covalent Organic Frameworks for Mercury Removal from Acidic Waste Water, *J. Hazard. Mater.*, 2020, **389**, 121824, DOI: **10.1016/j.jhazmat.2019.121824**.

67 L. Yang, Q. Guo, H. Kang, R. Chen, Y. Liu and D. Wei, Self-Controlled Growth of Covalent Organic Frameworks by Repolymerization, *Chem. Mater.*, 2020, **32**(13), 5634–5640, DOI: **10.1021/acs.chemmater.0c01140**.

68 S. Daliran, M. Blanco, A. Dhakshinamoorthy, A. R. Oveisi, J. Alemán and H. García, Defects and Disorder in Covalent Organic Frameworks for Advanced Applications, *Adv. Funct. Mater.*, 2023, **34**(18), 2312912, DOI: **10.1002/adfm.202312912**.

69 J. Dong, X. Han, Y. Liu, H. Li and Y. Cui, Metal–Covalent Organic Frameworks(MCOFs): A Bridge Between Metal–Organic Frameworks and Covalent Organic Frameworks, *Angew. Chem., Int. Ed.*, 2020, **59**(33), 13722–13733, DOI: **10.1002/anie.202004796**.

70 A. Kuc, M. A. Springer, K. Batra, R. Juarez-Mosqueda, C. Wöll and T. Heine, Proximity Effect in Crystalline Framework Materials: Stacking-Induced Functionality in MOFs and COFs, *Adv. Funct. Mater.*, 2020, **30**(41), 1908004, DOI: **10.1002/adfm.201908004**.

71 A. J. Lopes Jesus and J. S. Redinha, Molecular Insight into the Amine-Water Interaction: A Combined Vibrational, Energetic and NBO/NEDA Study, *Comput. Theor. Chem.*, 2013, **1023**, 74–82, DOI: **10.1016/j.comptc.2013.09.006**.

72 J. Zhong, Y. Zhao, L. Li, H. Li, J. S. Francisco and X. C. Zeng, Interaction of the NH2 Radical with the Surface of a Water Droplet, *J. Am. Chem. Soc.*, 2015, **137**(37), 12070–12078, DOI: **10.1021/jacs.5b07354**.

73 M. Thommes, K. Kaneko, A. V. Neimark, J. P. Olivier, F. Rodriguez-Reinoso, J. Rouquerol and K. S. W. Sing, Physisorption of Gases, with Special Reference to the Evaluation of Surface Area and Pore Size Distribution (IUPAC Technical Report), *Pure Appl. Chem.*, 2015, **87**(9–10), 1051–1069, DOI: **10.1515/pac-2014-1117**.

74 J. L. Fenton, D. W. Burke, D. Qian, M. O. D. L. Cruz and W. R. Dichtel, Polycrystalline Covalent Organic Framework Films Act as Adsorbents, Not Membranes, *J. Am. Chem. Soc.*, 2021, **143**(3), 1466–1473, DOI: **10.1021/jacs.0c11159**.